UNIVERSITÀ DEGLI STUDI DI PADOVA

Dipartimento di Fisica e Astronomia “Galileo Galilei”

Corso di Laurea in Fisica

Tesi di Laurea

Una Linea Laser a 1550 nm per la Misura di Proprietà di Diffusione della Luce per Einstein Telescope

A 1550 nm Laser Line to Measure Light Scattering Properties for the Einstein Telescope

Relatore

Dott.ssa Livia Conti

Correlatore

Dott. Francesco Flocco

Laureando

Fabio Cimino

Anno Accademico 2024/2025

Sommario

La luce diffusa rappresenta una significativa fonte di rumore nei rivelatori interferometrici di onde gravitazionali, come LIGO, Virgo e il futuro Einstein Telescope. Ridurne la generazione e la ricombinazione con il fascio principale è essenziale per migliorare la sensibilità del rivelatore. Ciò richiede la caratterizzazione delle proprietà di diffusione della luce di materiali, rivestimenti e componenti ottici alla specifica lunghezza d'onda utilizzata.

Mentre LIGO e Virgo utilizzano laser a 1064 nm e 532 nm, l'interferometro a bassa frequenza di Einstein Telescope opererà probabilmente a 1550 nm. Presso il DFA e l'INFN di Padova è già operativo un apparato di misura della diffusione della luce alle lunghezze d'onda impiegate da LIGO e Virgo. Per contribuire alla ricerca relativa ad Einstein Telescope, tale apparato deve essere esteso per consentire misure alla nuova lunghezza d'onda.

In questa tesi si presenta la progettazione, la costruzione e la caratterizzazione di una nuova linea laser a 1550 nm, nonché la sua integrazione nell'apparato esistente. Un sistema di lenti è sviluppato per consentire la regolazione della dimensione del fascio incidente sul campione. La polarizzazione della luce viene sfruttata per variare la potenza del fascio in modo preciso e automatizzato. La modulazione del fascio combinata con l'amplificazione lock-in è impiegata per ridurre il rumore di fondo e migliorare la sensibilità. Infine, l'analisi di un campione di riferimento mostra il comportamento atteso, dimostrando che l'apparato è ora in grado di caratterizzare materiali e rivestimenti di interesse per Einstein Telescope.

Abstract

Stray light is a significant source of noise in laser interferometric gravitational-wave detectors such as LIGO, Virgo, and the upcoming Einstein Telescope. Minimizing its generation and its recoupling with the main beam is essential to improve detector sensitivity. This requires characterization of the light scattering properties of materials, coatings, and optical components at the specific wavelength in use.

While LIGO and Virgo employ lasers at 1064 nm and 532 nm, the low-frequency interferometer of the Einstein Telescope is expected to operate at 1550 nm. At the DFA and INFN of Padova, an experimental facility is already operational for scattering measurements at the LIGO and Virgo wavelengths. To support research relevant to the Einstein Telescope, this facility needs to be extended to include the new wavelength.

This thesis presents the design, implementation, and characterization of a new 1550 nm laser line, as well as its integration into the existing setup. A lens system is developed to enable tunable beam spot sizes on the sample. A precise and automated power control system is implemented using polarization-based techniques. Beam modulation combined with lock-in amplification is employed to suppress background noise and enhance sensitivity. Finally, measurements on a reference sample confirm the expected behavior, demonstrating that the facility is now capable of characterizing materials and coatings relevant to the Einstein Telescope.

Contents

Chapter 1

Introduction

On September 14, 2015, soon after Advanced LIGO began operations following a major upgrade, the first direct observation of gravitational waves (GWs) was made [1, 2]. The signal, named GW150914, originated from the coalescence of a binary black hole system. This groundbreaking detection, together with subsequent observations from the international network of GW detectors, confirmed a key prediction of general relativity (GR) and demonstrated the feasibility of GW astronomy.

Despite this success, the sensitivity of current detectors remains insufficient to fully realize the scientific potential of GW astronomy. To transition from the era of detection to one of high-precision measurement, next-generation observatories are being planned. Within Europe, the Einstein Telescope (ET) is a proposed third-generation ground-based GW observatory set to outperform current detectors in all performance metrics. With an order of magnitude increase in both sensitivity and frequency range compared to current detectors, ET will enable detailed studies of black holes and neutron stars, uncover new astrophysical sources of GWs, provide insights into the early universe, look for dark matter and dark energy, test GR and other theories in fundamental physics to unprecedented levels [3].

To build a third-generation GW observatory, it is necessary to overcome the limitations of the technologies used in current interferometers. Given that typical GW induced strains are on the order of 10^{-22}, numerous factors contribute to the overall noise profile of an interferometer, each impacting the detector's sensitivity differently across the frequency spectrum of the GWs being observed. Figure 1.1 shows an example of the spectral noise distribution in Advanced Virgo.

Noise contributions are categorized as either fundamental or technical. Fundamental contributions include Newtonian, seismic, thermal, and quantum noise, while technical noise arises from instrumental effects, such as stray light.

Newtonian noise stems from fluctuations in the local gravitational field caused by numerous sources, such as human activity, atmospheric pressure changes, and seismic waves [5, 6]. Such fluctuations can lead to mirror displacements that are difficult to shield against. These same sources may also induce ground vibrations, in which case they are classified as seismic noise and can be mitigated by using suspension systems [7].

Thermal noise originates from random displacements of the mirror surfaces caused by thermal agitation of the coatings, substrates, and suspensions. It typically dominates between 50 Hz and 200 Hz, and poses a major challenge in room-temperature interferometers [8].

Quantum noise consists of two components: radiation pressure noise and shot noise. Radiation pressure arises from quantum mechanical amplitude fluctuations of the light field and causes random displacements of the mirrors. Shot noise, or quantum phase noise, stems from the statistical fluctuations in photon arrival times at the photodetector and limits the precision of phase difference measurements. Radiation pressure noise increases with the optical power incident on the mirror, whereas shot noise decreases as optical power increases. One of the two effects can be reduced at the expense of the other using quantum states of light known as squeezed light [9].

Stray light refers to unwanted light that deviates from the intended optical path and recombines with the primary beam. Sources of stray light include scattering from particulates or rough surfaces, clipping by finite apertures, or spurious reflections from imperfect anti-reflective coatings. To mitigate

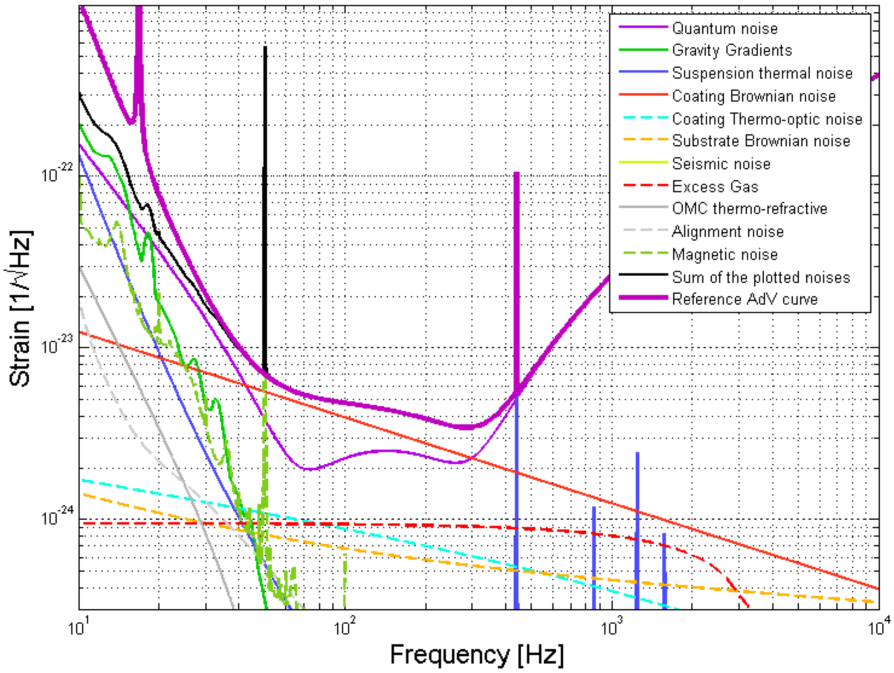

Figure 1.1: Spectral distribution of the main noise contributions in Advanced Virgo. Source: [4].

this effect, interferometers employ baffles—structures placed along the beam path or around optics—to absorb stray light before it can re-enter the main beam [10, 11].

To address these limitations, ET introduces several fundamental changes in design [12]. Unlike LIGO and Virgo, which use L-shaped geometries, ET will consist of three nested detectors arranged in an equilateral triangular configuration. Each side of the triangle will be 10 km long—significantly longer than the 3 km arms of Virgo and the 4 km arms of LIGO. Each detector will house two distinct interferometers optimized for different frequency bands [13]. This configuration, known as the "xylophone" design, is shown in Figure 1.2. One interferometer (ET-LF) will be optimized for low frequencies (3 Hz to 30 Hz), while the other (ET-HF) will target higher frequencies. ET-HF will use high optical powers—on the order of megawatts—to suppress shot noise, while ET-LF will operate at cryogenic temperatures (10 K to 20 K) and low powers to minimize thermal noise and radiation pressure. In both interferometers, appropriate squeezed light will be employed to reduce the complementary quantum noise source.

ET-LF will use silicon as the substrate material for its main optics, replacing fused silica—which has been extensively used in first and second generation detectors—due to its high mechanical losses at cryogenic temperatures [15]. Silicon is available in high quality due to its widespread use in the semiconductor industry and has excellent thermal and mechanical properties for cryogenic applications [16]. However, silicon is opaque at the wavelengths of 532 nm and 1064 nm used in current detectors. Therefore, ET-LF will operate at a longer wavelength, most likely 1550 nm, where silicon is transparent and exhibits low absorption ($< 5\,\mathrm{ppm\,cm^{-1}}$) [17], minimal birefringence ($\Delta n \approx 10^{-7}$) [18], negligible nonlinear effects [19], and an almost zero coefficient of thermal expansion [20, 21]. Squeezed light sources are also readily available at this wavelength [22].

Because optical properties are wavelength-dependent, the shift to 1550 nm requires characterization of the light scattering properties of new materials used in coatings, baffles, and other components. The DFA and INFN of Padova currently operate a scattering measurement facility that includes both a scatterometer and an integrating sphere. These instruments are used to characterize materials and coatings for use in LIGO, Virgo, and ET-HF at 532 nm and 1064 nm, specifically to measure the bidirectional scattering distribution function (BSDF) and the total integrated scattering (TIS), as described in Section 2.2. The setup allows control over laser power, polarization, and beam spot size (as defined in Section 2.1) on the sample to be characterized.

This thesis focuses on the integration of a new 1550 nm laser line into the existing setup. The work is limited to the scatterometer, with the integrating sphere to be addressed in future work. The

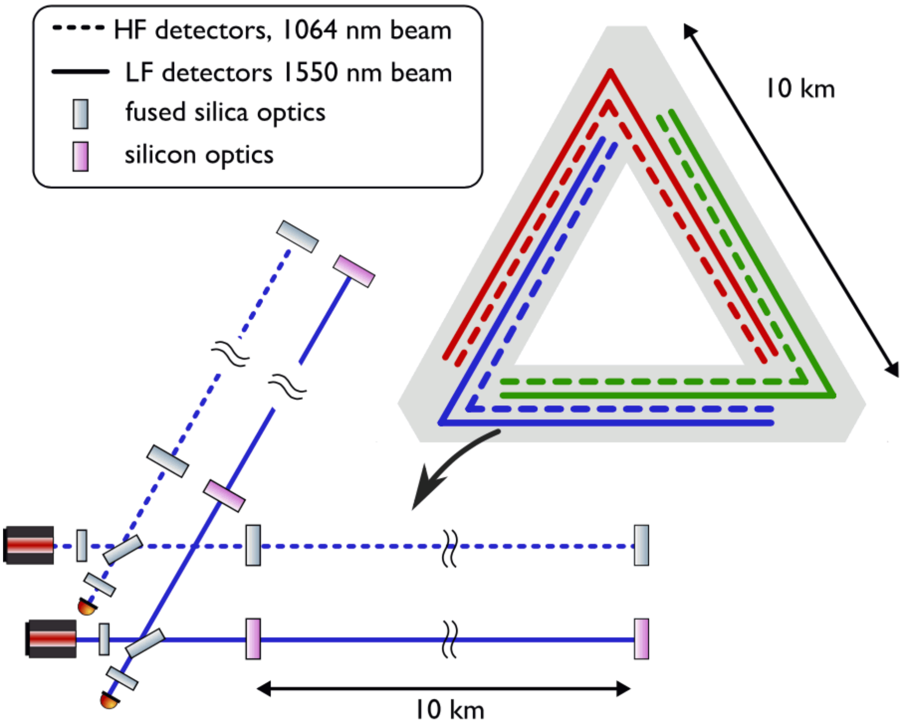

Figure 1.2: ET will consist of three detectors arranged in an equilateral triangle with 10 km sides. Each detector will contain two interferometers: one optimized for high frequencies (HF) and the other for low frequencies (LF). Source: [14].

upgrade is an essential step toward enabling material characterizations at the wavelength required by ET-LF.

Power control is achieved using a waveplate, which rotates the polarization of the incoming light, combined with a polarizing beam splitter that deflects light selectively based on polarization. A quasi-transparent window is also employed to monitor the circulating power by sampling the small reflected portion of the beam. An additional waveplate can be used to modify the final polarization state, but has not been implemented as part of this thesis work. The beam shape is adjusted using a specifically designed movable lens system, while a mechanical chopper modulates it at a set frequency. This allows a lock-in amplifier to reduce noise at other frequencies by demodulating the signal.

Chapter 2 establishes the theoretical background for this work, covering essential concepts related to Gaussian beam optics and the scattering properties of materials. It further introduces the working principle of the scatterometer, discusses the noise sources that affect its measurements, and outlines the basics of lock-in amplification for noise reduction. Chapter 3 documents the detailed design and implementation of all setup components, along with their expected performance. Chapter 4 presents experimental measurements of beam parameters and background noise levels, and compares them with these expectations. The chapter concludes with the analysis of a reference sample, demonstrating the scatterometer's performance in real measurement scenarios at 1550 nm.

Chapter 2

Theoretical Background

2.1 Gaussian beams

2.1.1 Overview

The propagation of electromagnetic waves in linear, homogeneous, isotropic, and source-free media with refractive index n is governed by the wave equation for the electric field $\mathbf{E}$:

$$\nabla^2 \mathbf{E} = \frac{1}{(c/n)^2} \frac{\partial^2 \mathbf{E}}{\partial t^2}. \tag{2.1}$$

The magnetic field $\mathbf{B}$ is then determined by the Maxwell–Faraday equation.

The electromagnetic field of a laser can be described under three simplifying approximations [23]. First, the wave is assumed to be monochromatic with angular frequency ω. The electric field can then be expressed in phasor notation as

$$\mathbf{E}(\mathbf{r}, t) = \Re\left[\tilde{\mathbf{E}}(\mathbf{r}) e^{-i\omega t}\right]. \tag{2.2}$$

Second, the paraxial approximation is applied, meaning that the wave propagates at small angles relative to the optical axis—say, the z-axis. Under these conditions, a well-defined wave vector $\mathbf{k} = \frac{n\omega}{c}\hat{\mathbf{z}}$ can be introduced. Denoting its magnitude by $k = |\mathbf{k}|$, the wave equation reduces to the vector Helmholtz equation:

$$(\nabla^2 + k^2)\tilde{\mathbf{E}} = \mathbf{0}. \tag{2.3}$$

The third approximation is the slowly varying envelope approximation (SVEA), for which

$$\tilde{\mathbf{E}}(x, y, z) = u(x, y, z) e^{-ikz} \hat{\mathbf{e}}, \tag{2.4}$$

where $\hat{\mathbf{e}}$ denotes the polarization of the field, and the envelope u varies slowly along z compared with the carrier wave e^{-ikz}. Substituting this expression into Equation 2.3 and neglecting $\frac{\partial^2 u}{\partial z^2}$ yields the paraxial Helmholtz equation:

$$\frac{\partial^2 u}{\partial x^2} + \frac{\partial^2 u}{\partial y^2} - 2ik\frac{\partial u}{\partial z} = 0. \tag{2.5}$$

The solutions of Equation 2.5, when substituted into Equation 2.2, describe Gaussian beams. These solutions can be decomposed in several complete sets of orthogonal modes. Two of the most common are the Hermite–Gaussian and Laguerre–Gaussian modes. It can be shown that certain optical resonators can sustain either Hermite–Gaussian or Laguerre–Gaussian modes, depending on their geometry. Lasers based on these resonators can thus emit Gaussian beams. In most cases, the intended output is the fundamental, or TEM_{00}, mode, which is the lowest-order mode of both the Hermite–Gaussian and Laguerre–Gaussian families. Its envelope is given by

$$u(x, y, z) = u_0 \sqrt{\frac{q_{0x} q_{0y}}{q_x(z) q_y(z)}} \exp\left[-i\frac{k}{2}\left(\frac{x^2}{q_x(z)} + \frac{y^2}{q_y(z)}\right)\right], \tag{2.6}$$

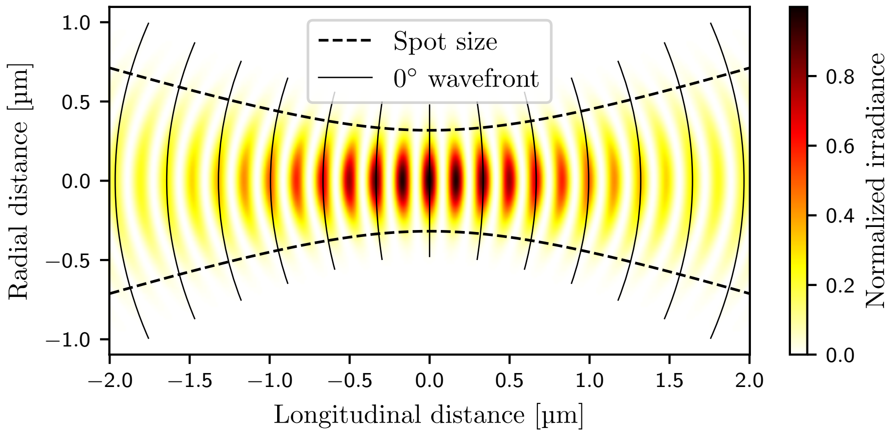

Figure 2.1: Instantaneous irradiance distribution of a Gaussian beam with a circular cross-section, where $\lambda = w_0 = 318\,\mathrm{nm}$, $n = 1$, and $z_\mathrm{R} = 1\,\mathrm{\mu m}$. As time progresses, the wavefronts propagate to the left or right at the speed of light in the medium. Source code available.

where $q_x(z)$, $q_y(z)$ are the complex beam parameters in the x and y directions, and u_0 is a positive amplitude factor. This beam exhibits a Gaussian field amplitude distribution in the transverse plane across the entire optical axis. The standard deviation in direction $j \in \{x, y\}$ is denoted $w_j(z)$ and called the spot size. Each spot size has a minimum w_{0j} called the waist size and located at the waist position z_{0j}. The same notation was used in Equation 2.6 for the complex parameter at the waist position $q_{0j} = q(z_{0j})$.

Defining the Rayleigh range as $z_{\mathrm{R}j} = \frac{\pi w_{0j}^2 n}{\lambda}$, with λ the vacuum wavelength, it can be shown that $q_j(z) = (z - z_{0j}) + i z_{\mathrm{R}j}$, that is the Gaussian beam is completely specified by either the complex parameters or the waist sizes and positions. Substituting this expression in Equation 2.6 leads to a more intuitive formula for the envelope:

$$u(x, y, z) = \underbrace{u_0 \sqrt{\frac{w_{0x} w_{0y}}{w_x(z) w_y(z)}} \exp\left[-\frac{x^2}{w_x^2(z)} - \frac{y^2}{w_y^2(z)}\right]}_{\text{amplitude term}} \underbrace{\exp\left[-i\frac{k}{2}\left(\frac{x^2}{R_x(z)} + \frac{y^2}{R_y(z)}\right)\right]}_{\text{transverse phase factor}} \underbrace{\exp[i\zeta(z)]}_{\substack{\text{longitudinal} \\ \text{phase factor}}} . \tag{2.7}$$

Here, $R_j(z)$ is the radius of curvature of the wavefront at position z, while $\zeta(z)$ is a phase term called Gouy phase. In terms of the waist size and position:

$$w_j(z) = w_{0j} \sqrt{1 + \left(\frac{z - z_{0j}}{z_{\mathrm{R}j}}\right)^2}, \tag{2.8}$$

$$R_j(z) = (z - z_{0j}) \left[1 + \left(\frac{z_{\mathrm{R}j}}{z - z_{0j}}\right)^2\right], \tag{2.9}$$

$$\zeta(z) = \frac{\arctan\left(\frac{z - z_{0x}}{z_{\mathrm{R}x}}\right) + \arctan\left(\frac{z - z_{0y}}{z_{\mathrm{R}y}}\right)}{2}. \tag{2.10}$$

The spot size follows a hyperbolic dependence on z, approaching linear growth in the far field. At the waist and at infinity, the wavefront is planar, while at intermediate positions it is spherical. The minimum radius of curvature occurs at $z = z_{0j} \pm z_{\mathrm{R}j}$, i.e. one Rayleigh range from the waist. The Gouy phase introduces a phase shift of π radians as one moves from the far field on one side of the waist to the far field on the other side.

The instantaneous irradiance distribution of the beam is proportional to the square of the real electric field in Equation 2.2:

$$I(x, y, z) = I_0 \frac{w_{0x} w_{0y}}{w_x(z) w_y(z)} \exp\left(-\frac{2x^2}{w_x^2(z)} - \frac{2y^2}{w_y^2(z)}\right) \cos^2\left[-kz - \frac{k}{2}\left(\frac{x^2}{R_x(z)} + \frac{y^2}{R_y(z)}\right) + \zeta(z) - \omega t\right]. \tag{2.11}$$

Since typical detectors cannot resolve optical frequencies, the measured irradiance corresponds to the time-averaged value:

$$I'(x,y,z) = I'_0 \frac{w_{0x} w_{0y}}{w_x(z) w_y(z)} \exp\left(-\frac{2x^2}{w_x^2(z)} - \frac{2y^2}{w_y^2(z)} \right). \tag{2.12}$$

The beam spot size has been defined as the standard deviation of the field amplitude distribution. Therefore, the spot size $w_j(z)$ describes the distance at which the beam's irradiance drops to $1/e^2$ of its maximum value in the transverse direction j. The beam irradiance profile can be elliptical if $w_{0x} \neq w_{0y}$ or if $z_{0x} \neq z_{0y}$. When the latter condition occurs, the beam is said to be astigmatic. Figure 2.1 illustrates the instantaneous irradiance distribution of an ideal Gaussian beam with equal waist sizes and positions in the two transverse directions.

2.1.2 Propagation through arbitrary optical systems

In geometrical optics, ray tracing under the paraxial approximation can be performed using ray transfer matrix analysis—also known as ABCD matrix analysis [24]. This formalism assigns a 2×2 matrix to each optical element or segment of beam propagation. The matrix acts on a vector representing the incident ray, yielding the vector corresponding to the outgoing ray.

In geometrical optics, the ray vector comprises two components: the transverse position relative to the optical axis, and the angle the ray makes with that axis. By multiplying matrices corresponding to successive optical elements, one can describe complex optical systems as a single ray transfer matrix. For instance, the ray transfer matrix of a thick lens can be expressed as the product of three matrices: refraction at the first curved surface, propagation through the lens medium, and refraction at the second curved surface. Table 2.1 summarizes the ray transfer matrices for common optical interfaces and elements.

The same matrices can be used to compute the evolution of Gaussian beams through optical systems. In this context, however, the transformation of the beam is not obtained through direct matrix–vector multiplication. Instead, the evolution of a Gaussian beam through an optical system characterized by the matrix $\begin{pmatrix} A & B \\ C & D \end{pmatrix}$ is governed by the transformation of the complex beam parameter:

$$q_{\text{out}} = \frac{A q_{\text{in}} + B}{C q_{\text{in}} + D}, \tag{2.13}$$

where q_{in} and q_{out} denote the complex beam parameters before and after the optical system, respectively.

Table 2.1: Ray transfer matrices for common optical interfaces and elements [24].

Element	**Matrix**	**Remarks**
Propagation in a medium	$\begin{pmatrix} 1 & d \\ 0 & 1 \end{pmatrix}$	d = propagation distance, constant refractive index.
Refraction at a flat interface	$\begin{pmatrix} 1 & 0 \\ 0 & \frac{n_1}{n_2} \end{pmatrix}$	n_1 = initial refractive index, n_2 = final refractive index.
Reflection from a flat mirror	$\begin{pmatrix} 1 & 0 \\ 0 & 1 \end{pmatrix}$	
Refraction at a curved interface	$\begin{pmatrix} 1 & 0 \\ \frac{n_1 - n_2}{n_2 R} & \frac{n_1}{n_2} \end{pmatrix}$	n_1 = initial refractive index, n_2 = final refractive index, R = radius of curvature.
Thin lens	$\begin{pmatrix} 1 & 0 \\ -\frac{1}{f} & 1 \end{pmatrix}$	f = focal length.
Thick lens	$\begin{pmatrix} 1 & 0 \\ \frac{n_2 - n_1}{n_1 R_2} & \frac{n_2}{n_1} \end{pmatrix} \begin{pmatrix} 1 & t \\ 0 & 1 \end{pmatrix} \begin{pmatrix} 1 & 0 \\ \frac{n_1 - n_2}{n_2 R_1} & \frac{n_1}{n_2} \end{pmatrix}$	n_1 = external refractive index, n_2 = lens refractive index, t = center thickness, R_1, R_2 = radii of curvature.

2.2 Scattering properties of materials

The propagation of electromagnetic waves through a medium is influenced by absorption, emission, and scattering processes.

- Absorption reduces the radiant flux of the wave by converting it into other forms of energy, such as heat.
- Emission increases the radiant flux via spontaneous or stimulated emission processes, which may occur in luminescent materials.
- Scattering redistributes radiance in different directions through interactions with inhomogeneities, either at material boundaries (surface scattering) or within the bulk medium (volume scattering). This section provides an overview of these mechanisms.

2.2.1 Surface scattering

Surface scattering occurs when an incident wave interacts with the boundary between two media of different refractive indices. Under idealized conditions, reflection and refraction are fully described by Fresnel's equations and Snell's law, which depend on the angle of incidence and the light's polarization. Real surfaces, however, deviate from this ideal behavior due to microscopic roughness and the presence of scattering centers beneath the surface [25, 26].

The angular redistribution of scattered radiation is characterized by the bidirectional scattering distribution function (BSDF). In spherical coordinates, the incident and scattering directions are specified by the zenith and azimuthal angles $(\theta_\mathrm{i}, \varphi_\mathrm{i})$ and $(\theta_\mathrm{s}, \varphi_\mathrm{s})$ as illustrated in Figure 2.2. The BSDF is then defined as

$$\mathrm{BSDF}(\theta_\mathrm{i}, \varphi_\mathrm{i}, \theta_\mathrm{s}, \varphi_\mathrm{s}) = \frac{\mathrm{d}L(\theta_\mathrm{i}, \varphi_\mathrm{i}, \theta_\mathrm{s}, \varphi_\mathrm{s})}{\mathrm{d}I(\theta_\mathrm{i}, \varphi_\mathrm{i})}, \tag{2.14}$$

where $I(\theta_\mathrm{i}, \varphi_\mathrm{i})$ is the irradiance incident upon the surface, and $L(\theta_\mathrm{i}, \varphi_\mathrm{i}, \theta_\mathrm{s}, \varphi_\mathrm{s})$ is the radiance scattered in the direction $(\theta_\mathrm{s}, \varphi_\mathrm{s})$, that is the radiant flux leaving the surface per unit solid angle per unit projected area in that direction. Physically realizable BSDFs satisfy the Helmholtz reciprocity principle, meaning that they are invariant under exchange of incident and scattered directions—hence the term "bidirectional". The BSDF may depend on the wavelength and polarization state of the incident radiation. Furthermore, spatial inhomogeneities in the material may lead to position-dependent scattering behavior. As such, the BSDF should be regarded as a sample-specific property rather than an intrinsic material property.

The BSDF is typically decomposed into a reflected component, the bidirectional reflectance distribution function (BRDF), and a transmitted component, the bidirectional transmittance distribution function (BTDF). Figure 2.3 illustrates example BRDFs.

In the experimental facility discussed in this thesis, the BSDF of a sample is measured by the scatterometer, whose working principle is explained in Section 2.3.1. Scattering can also be quantified by the total integrated scatter (TIS), defined as the fraction of incident optical power scattered into a

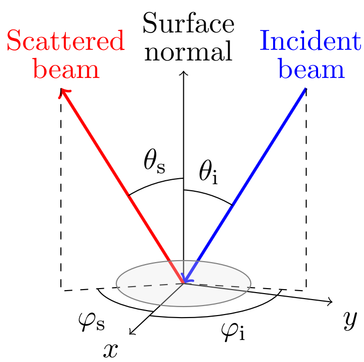

Figure 2.2: Illustration of the incident and scattered directions used in the BSDF definition. The sample lies in the x-y plane and is represented by the gray patch.

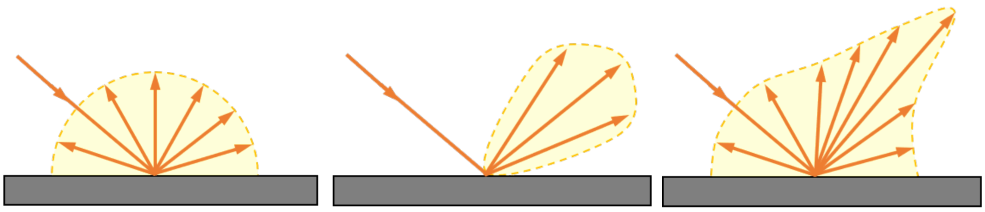

Figure 2.3: Example BRDFs: shown from left to right are a diffuse surface, a glossy surface, and a surface characterized by a more general BRDF. The BRDF value is represented by the length of the vector. Source: [27].

hemisphere. The TIS can be measured directly using an integrating sphere, or equivalently, obtained by integrating the BSDF over a hemisphere. For reflection:

$$\mathrm{TIS}(\theta_\mathrm{i}, \varphi_\mathrm{i}) = \int_0^{2\pi} \mathrm{d}\varphi_\mathrm{s} \int_0^{\pi/2} \mathrm{d}\theta_\mathrm{s} \mathrm{BSDF}(\theta_\mathrm{i}, \varphi_\mathrm{i}, \theta_\mathrm{s}, \varphi_\mathrm{s}) \cos(\theta_\mathrm{s}) \sin(\theta_\mathrm{s}). \tag{2.15}$$

The $\sin(\theta_\mathrm{s})$ term accounts for the differential area element on the unit sphere, while the $\cos(\theta_\mathrm{s})$ factor adjusts for projected area when computing irradiance contributions from different scattering angles.

2.2.2 Volume scattering

Volume scattering occurs when light interacts with inhomogeneities within the bulk of a medium. The scattering behavior depends on the ratio of the inhomogeneity size d to the wavelength λ [28].

When the inhomogeneity size d is much smaller than the wavelength λ, scattering is well described by Rayleigh theory. In this regime, the incident electric field drives the charges within it to oscillate at the same frequency, so that the inhomogeneity acts like a radiating dipole. The radiation emitted by this dipole is observed as scattered light. For a spherical inhomogeneity of radius r and refractive index n, the scattered irradiance I_s at an observation point a distance R away is

$$I_\mathrm{s} = I_\mathrm{i} \frac{8\pi^4 r^6}{\lambda^4 R^2} \left(\frac{n^2 - 1}{n^2 + 1} \right)^2 \left(1 + \cos^2\theta\right), \tag{2.16}$$

where I_i is the incident irradiance and θ is the scattering angle. This expression may be written in terms of the polarizability volume of the inhomogeneity, α, using the Lorentz–Lorenz equation:

$$I_\mathrm{s} = I_\mathrm{i} \frac{8\pi^4 \alpha^2}{\lambda^4 R^2} \left(1 + \cos^2\theta\right). \tag{2.17}$$

The polarization of the scattered light depends on the scattering angle and becomes complete at $\theta = 90°$. When the incident light is already polarized, Equation 2.16 no longer applies, and more general expressions must be used to describe the scattering.

Rayleigh scattering is primarily responsible for the scattering of light in the atmosphere. Its strong wavelength dependence causes the irradiance of scattered blue light (450 nm to 495 nm) to be several times greater than that of red light (625 nm to 740 nm). Together with human color perception, this explains the color of the sky at different times of the day [29].

When the inhomogeneity size d is comparable to the wavelength λ, Mie scattering theory must be used. Although more general, Mie theory is mathematically more involved and reduces to Rayleigh scattering for inhomogeneities much smaller than the wavelength, or to geometrical optics for inhomogeneities much larger. Mie theory is necessary to explain phenomena such as the white appearance of clouds and the glare produced by dust, smoke, and atmospheric pollutants.

In the context of GW detectors, volume scattering occurs within the substrates of optical components, primarily in thick transmissive optics. In this case, its effects can be quantified using the BSDF by treating optical boundaries as effective scattering surfaces. In this thesis, volume scattering is relevant because it contributes to noise in the scatterometer setup, which operates in air and is therefore subject to Rayleigh scattering from air molecules, as described in Section 2.3.2.

2.3 BSDF measurements

2.3.1 Scatterometer

The BSDF of a sample can be measured using a scatterometer. The scatterometer consists of a sample holder, where the sample is positioned, and a rotatable detector that records scattered light. A Gaussian beam illuminates the sample surface, and the detector measures the power scattered in a specific direction.

Let $\mathrm{d}\Sigma$ denote an illuminated surface element, $\mathrm{d}P_\mathrm{i}$ the differential incident power on $\mathrm{d}\Sigma$, $\mathrm{d}P_\mathrm{s}$ the differential power scattered by $\mathrm{d}\Sigma$, and $\mathrm{d}\Omega$ a differential solid angle. The irradiance on the surface and the scattered radiance in direction $\mathrm{d}\Omega$ are given by

$$I = \frac{\mathrm{d}P_\mathrm{i}}{\mathrm{d}\Sigma}, \qquad L = \frac{\mathrm{d}^2 P_\mathrm{s}}{\mathrm{d}\Sigma \cos\theta_\mathrm{s} \mathrm{d}\Omega}, \tag{2.18}$$

respectively. Assuming that the sample response is directly proportional to incident irradiance, that is $L = CI$ for a constant C, the BSDF is given by

$$\mathrm{BSDF} = \frac{\mathrm{d}L}{\mathrm{d}I} = \frac{L}{I}. \tag{2.19}$$

If the detector captures all radiance leaving the surface, the measured power is

$$P_\mathrm{s} = \int_\Sigma \int_{\Omega_\mathrm{d}} \mathrm{d}^2 P_\mathrm{s} = \int_\Sigma \int_{\Omega_\mathrm{d}} \mathrm{BSDF} \cos\theta_\mathrm{s} I_\mathrm{i} \mathrm{d}\Omega \mathrm{d}\Sigma, \tag{2.20}$$

where Σ is the surface region contributing to scattering, and Ω_d is the solid angle subtended by the detector. Since the Gaussian beam has an exponentially decreasing irradiance profile, Σ can be taken as a small area that contains most of the incident optical power. For sufficiently small Σ, the BSDF can be assumed uniform. Furthermore, if the detector is far from the sample, the scattering direction $(\theta_\mathrm{s}, \varphi_\mathrm{s})$ can be taken constant for all scattering points in Σ. Under these conditions,

$$P_\mathrm{s} = \mathrm{BSDF} \cos\theta_\mathrm{s} \Omega_\mathrm{d} \int_\Sigma I_\mathrm{i} \mathrm{d}\Sigma = \mathrm{BSDF} \cos\theta_\mathrm{s} \Omega_\mathrm{d} P_\mathrm{i}, \tag{2.21}$$

thus the BSDF can be computed by the scatterometer as

$$\mathrm{BSDF}(\theta_\mathrm{i}, \varphi_\mathrm{i}, \theta_\mathrm{s}, \varphi_\mathrm{s}) = \frac{P_\mathrm{s}(\theta_\mathrm{i}, \varphi_\mathrm{i}, \theta_\mathrm{s}, \varphi_\mathrm{s})}{P_\mathrm{i} \cos\theta_\mathrm{s} \Omega_\mathrm{d}}. \tag{2.22}$$

Equation 2.19 assumes not only linearity but also the absence of noise-induced offsets. If noise is present, at scattering directions that are perpendicular to the surface, the projected area is zero, however the power recorded by the detector is not, causing a divergence in the BSDF computed via Equation 2.22. To mitigate this, the cosine-corrected BSDF is often used:

$$\mathrm{cBSDF}(\theta_\mathrm{i}, \varphi_\mathrm{i}, \theta_\mathrm{s}, \varphi_\mathrm{s}) = \mathrm{BSDF}(\theta_\mathrm{i}, \varphi_\mathrm{i}, \theta_\mathrm{s}, \varphi_\mathrm{s}) \cos(\theta_\mathrm{s}).$$

2.3.2 Noise in BSDF measurements

Noise in BSDF measurements arises from two main sources: stray light and electronic noise in the photoelectronic readout. If noise power P_noise is recorded by the scatterometer during a measurement, the measured cBSDF differs from the true cBSDF:

$$\mathrm{cBSDF}_\mathrm{measured}(\theta_\mathrm{i}, \varphi_\mathrm{i}, \theta_\mathrm{s}, \varphi_\mathrm{s}) = \mathrm{cBSDF}_\mathrm{true}(\theta_\mathrm{i}, \varphi_\mathrm{i}, \theta_\mathrm{s}, \varphi_\mathrm{s}) + \frac{P_\mathrm{noise}}{P_\mathrm{i} \Omega_\mathrm{d}}. \tag{2.23}$$

Within the scatterometer, stray light originates from unwanted surface scattering and clipping on optical elements, ambient light leaking into the system, and volume scattering from the surrounding environment.

Clipping occurs when the light beam overfills the finite apertures of the optical elements. This effect is quantified by the clipping factor, defined as the ratio of the power transmitted through an aperture to the total beam power. In the experimental setup considered, clipping is neglected when this factor falls below 10^{-6}.

The scatterometer operates in air, therefore Rayleigh scattering from air molecules occurs. Starting from Equation 2.16, which describes the irradiance scattered by a single molecule, models can be developed to quantify the expected noise in the scatterometer described in this section [30, 31]. If the detector is positioned at a distance R from the sample, and has a field of view γ, the scatterometer measures the scattered light as

$$\mathrm{cBSDF}(\theta_\mathrm{s}) = \left(\frac{2\pi}{\lambda}\right)^4 \rho_N \alpha^2 \int_{-l_1(\theta_\mathrm{s})}^{l_2(\theta_\mathrm{s})} \frac{R^2}{R^2 + z^2 - 2Rz\cos\theta_\mathrm{s}} \mathrm{d}z \tag{2.24}$$

where the integration limits $l_1(\theta_\mathrm{s}) = R\frac{\sin\gamma}{\sin(\theta_\mathrm{s}+\gamma)}$ and $l_2(\theta_\mathrm{s}) = R\frac{\sin\gamma}{\sin(\theta_\mathrm{s}-\gamma)}$ correspond to the portion of the beam within the detector's field of view, ρ_N denotes the number density of air molecules, and α is their volume polarizability.

Several strategies can mitigate stray light within the scatterometer, such as operating in vacuum, employing anti-reflection coatings, using baffles to block off-axis scatter, blackening mechanical surfaces, using beam dumps to terminate unused beams, and enclosing the system in light-tight housing to shield it from ambient light.

Electronic noise arises from both the photodetector and the subsequent measurement circuitry. At low frequencies, noise sources can be roughly divided into flicker noise and white noise. Flicker noise, also known as 1/f noise, has a power spectral density that decreases approximately inversely with frequency and arises primarily from defects in the semiconductor materials. White noise, in contrast, exhibits a flat power spectral density and contributes equally across all frequencies. It is mainly caused by thermal agitation in resistive elements (Johnson–Nyquist noise) and by shot noise resulting from the discrete nature of charge carriers.

2.3.3 Lock-in amplifier for noise reduction

The frequency dependence of noise sources can be exploited to reduce noise in BSDF measurements. By modulating the laser beam, the spectral content of the input signal to the detector can be shifted from DC to a frequency where the noise power spectral density is lower. Flicker noise decreases with frequency, and stray light not originating from the input beam has little spectral content at the modulation frequency. Measuring the detector output within a narrow bandwidth centered at the modulation frequency effectively rejects many noise contributions. An instrument that implements this detection scheme is the lock-in amplifier.

A lock-in amplifier consists of two mixers followed by two low-pass filters. Consider a sinusoidally modulated signal of amplitude V_s, angular frequency ω_s, and phase φ_s. The input voltage at the lock-in amplifier is composed of the signal and the noise $n(t)$:

$$V_\mathrm{in}(t) = V_\mathrm{s}\sin(\omega_\mathrm{s}t + \varphi_\mathrm{s}) + n(t). \tag{2.25}$$

The input signal is first split and then fed into the two mixers as shown in Figure 2.4. The mixers multiply the input signal by a reference sinusoidal wave. In the first mixer, the reference has amplitude V_r, angular frequency ω_s, and phase φ_r, while in the second mixer the reference has an additional 90° phase. Using trigonometric product identities, the multiplied signals are:

$$\begin{aligned} V_\mathrm{mul,1}(t) &= V_\mathrm{in}(t)V_\mathrm{r}\sin(\omega_\mathrm{s}t + \varphi_\mathrm{r}) \\ &= \frac{1}{2}V_\mathrm{s}V_\mathrm{r}\left[\cos(\varphi_\mathrm{s} - \varphi_\mathrm{r}) - \cos(2\omega_\mathrm{s}t + \varphi_\mathrm{s} + \varphi_\mathrm{r})\right] + V_\mathrm{r}n(t)\sin(\omega_\mathrm{s}t + \varphi_\mathrm{r}), \end{aligned} \tag{2.26}$$

$$\begin{aligned} V_\mathrm{mul,2}(t) &= V_\mathrm{in}(t)V_\mathrm{r}\sin(\omega_\mathrm{s}t + \varphi_\mathrm{r} + 90^\circ) \\ &= \frac{1}{2}V_\mathrm{s}V_\mathrm{r}\left[\sin(2\omega_\mathrm{s}t + \varphi_\mathrm{s} + \varphi_\mathrm{r}) + \sin(\varphi_\mathrm{s} - \varphi_\mathrm{r})\right] + V_\mathrm{r}n(t)\cos(\omega_\mathrm{s}t + \varphi_\mathrm{r}) \end{aligned} \tag{2.27}$$

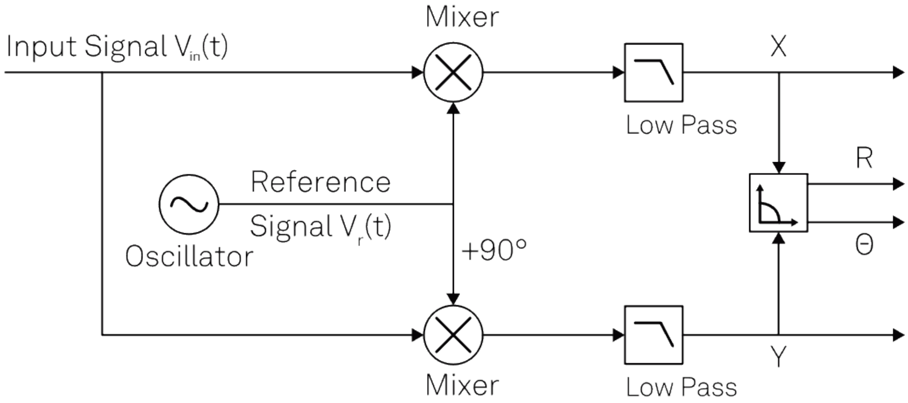

Figure 2.4: Schematic of a lock-in amplifier. Source: [32].

The low-pass filters remove the AC components of the multiplied signals. If the noise $n(t)$ has negligible spectral content near the reference frequency, it is effectively suppressed. The resulting filtered signals correspond to the in-phase (X) and quadrature (Y) components:

$$X = \frac{1}{2} V_\mathrm{s} V_\mathrm{r} \cos(\theta), \qquad Y = \frac{1}{2} V_\mathrm{s} V_\mathrm{r} \sin(\theta), \tag{2.28}$$

where $\theta = \varphi_\mathrm{s} - \varphi_\mathrm{r}$ is the phase difference between the signal and the reference. The lock-in amplifier outputs both the amplitude R and the phase θ:

$$R = \sqrt{X^2 + Y^2}, \qquad \theta = \arctan \frac{Y}{X}. \tag{2.29}$$

The signal amplitude can then be recovered as

$$V_\mathrm{s} = \frac{2R}{V_\mathrm{r}}, \tag{2.30}$$

which is independent of the phase difference between the reference and the signal.

Lock-in amplifiers can also handle square-wave modulated signals. In this case, the lock-in amplifier detects the square-wave frequency ω_0 and generates sinusoidal references at that frequency. The input signal can be expressed as a Fourier series

$$V_\mathrm{in} = V_\mathrm{s} \frac{4}{\pi} \sum_{k=0}^{\infty} \frac{1}{2k+1} \sin((2k+1)\omega_0 t) + n(t). \tag{2.31}$$

Only the fundamental harmonic is preserved by the lock-in amplifier, thus the signal amplitude is recovered as

$$V_\mathrm{s} = \frac{\pi R}{2V_\mathrm{r}}. \tag{2.32}$$

Chapter 3

Design and Implementation of the Laser Line

This chapter presents the design and implementation of the new 1550 nm laser line developed as part of this thesis. The laser line was integrated into the existing setup that already accommodated two laser lines at 532 nm and 1064 nm. As with the existing sources, the 1550 nm beam can be routed toward different measurement instruments: a scatterometer for determining the BSDF, or an integrating sphere for measuring the TIS. The optical layouts at the beginning and end of this work are shown in Figure 3.1 and described in this chapter.

Throughout this thesis, the new line is employed exclusively with the scatterometer. Within this setup, the main objectives of all laser lines are: (i) steering the beam towards the sample under analysis, (ii) controlling the optical power at the sample, (iii) adjusting the beam spot size, and (iv) setting the desired polarization state of the light. The scatterometer can then record the light scattered by the sample. The 1550 nm laser line achieves these objectives by replicating the key techniques used in the other lines, with necessary adaptations for its wavelength. An overview of these is provided here, followed by detailed specifications in the subsequent sections.

Switching between wavelengths, or between the scatterometer and the integrating sphere, is accomplished using flip mirrors (FMs), which direct the beam from the chosen source to a common beam path. A periscope raises the beam to the height required by the scatterometer.

Laser power is controlled using a half-wave plate (HWP) in combination with a polarizing beam splitter (PBS). The HWP rotates the polarization of the incident linearly polarized beam, while the PBS transmits or reflects light depending on its polarization state. By adjusting the HWP orientation, the transmitted power can be continuously varied from nearly zero up to the laser's maximum output of approximately 500 mW. A beam sampler (BS) positioned after the PBS reflects a small fraction of the light to a monitoring photodiode (PD), which generates a voltage signal proportional to the incident optical power. After calibration, the photodiode signal provides a direct measure of the circulating laser power, enabling real-time monitoring during operation.

Beam spot size at the sample is adjusted using a telescope system composed of three lenses (L1, L2, and L3). One of the lenses is mounted on a translation stage, allowing the spot size to be varied from approximately 400 µm to 2000 µm without beam clipping at intermediate optics.

An additional HWP can be placed after the PBS to enable arbitrary control of the linear polarization state of light incident on the sample. Furthermore, a polarizer can be mounted in front of the scatterometer's photodiode, allowing measurement of the BSDF under different combinations of incident and scattered polarization states.

Noise reduction in the system relies on both passive and active methods. Passive measures include a beam dump to terminate the laser beam, black absorptive panels to isolate optical areas, and iris diaphragms to limit stray light. Active suppression is achieved through optical power modulation and lock-in demodulation, which rejects most noise sources not originating from the beam. The existing 532 nm and 1064 nm laser sources can be modulated by powering them with AC current. This is not possible with the 1550 nm source; therefore a mechanical chopper periodically interrupts the beam to generate square-wave modulation.

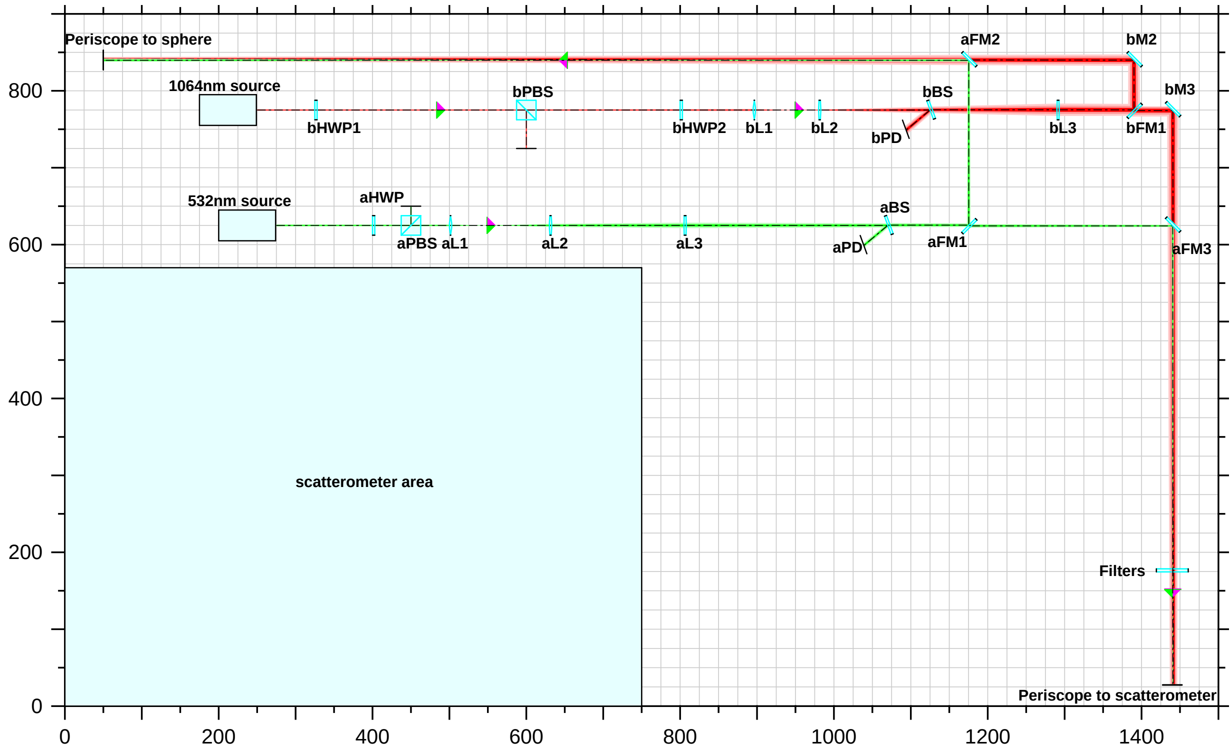

(a) Optical layout at the beginning of this thesis work.

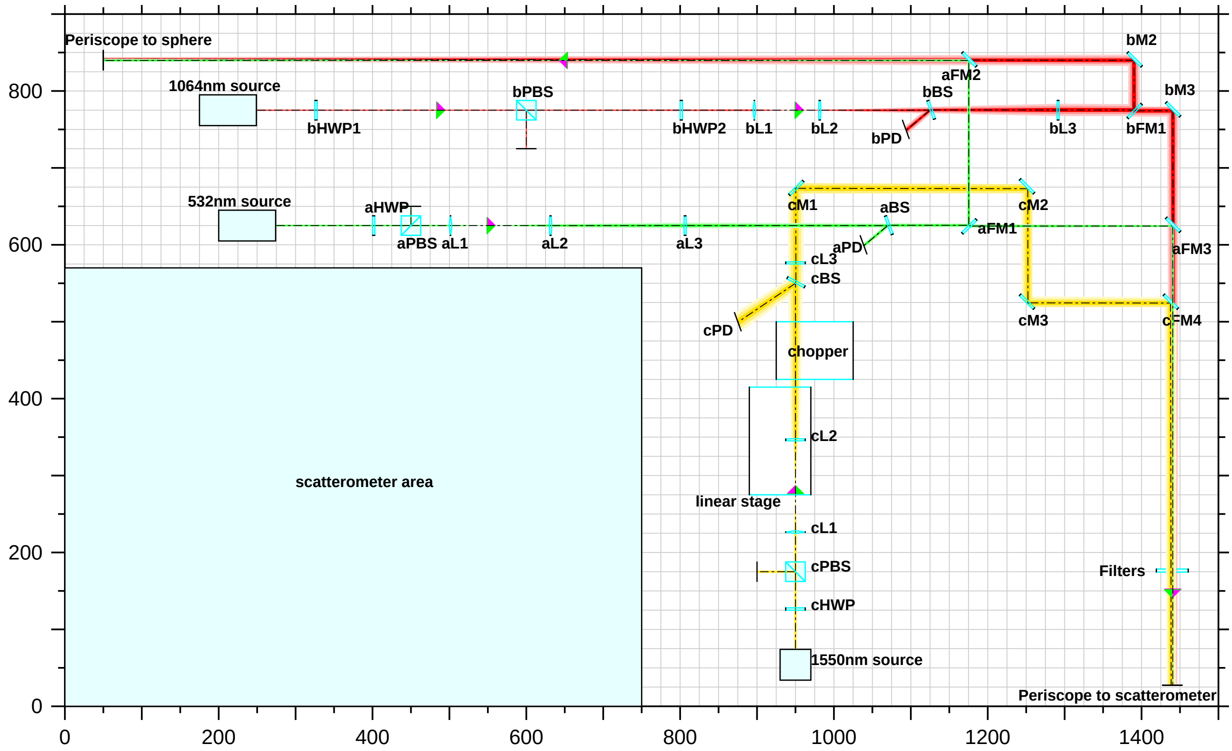

(b) Optical layout at the end of this thesis work.

Figure 3.1: Optical layout of the bottom level of the facility. The integrating sphere is on the top level, while the scatterometer spans both levels. Periscopes raise the beams to the required height. The 532 nm beam is shown in green, with components prefixed by 'a'. The 1064 nm and 1550 nm are instead in red and yellow, respectively, with components prefixed by 'b' and 'c'. The grid spacing of 25 mm corresponds to the spacing between the holes in the optical table. Axes indicate distances (in mm) from the bottom-left corner of the table. Abbreviations are: HWP = half-wave plate, PBS = polarizing beam splitter, L = lens (L1–L3), M = mirror, FM = flip mirror, PD = photodiode, BS = beam sampler. Layout created using the software Optocad [33].

3.1 Input beam characterization

The laser source emits linearly polarized, single-frequency light at 1550 nm. Light is delivered to the optical table through a fiber-optic cable and collimated using a beam collimator.

To design a telescope capable of producing spot sizes between 400 µm and 2000 µm at the sample, located approximately at 3 m from the collimator, the collimated beam must be first characterized. This characterization is performed by measuring the spot size at multiple positions along the propagation axis using a beam profiler. The resulting data are then fitted using Gaussian beam propagation theory to estimate the beam waist positions and sizes, as detailed in Section 2.1.

The beam profiler captures the full Gaussian irradiance profile of the beam and determines the beam diameter and centroid position along adjustable X and Y axes, which are aligned with the horizontal direction perpendicular to the laser beam and the vertical direction on the optical table, respectively.

Measured spot sizes along the propagation axis are plotted in Figure 3.2. The axial origin is defined at a reference hole on the optical table at coordinates (950, 75) in the optical layouts of Figure 3.1, approximately corresponding to the collimator position. The distance of 16.51 mm between the beam profiler casing and its photosensitive surface is accounted for in the analysis. Uncertainties in the axial position and beam diameter are 1 mm and 5 µm, respectively.

The observed difference between the X- and Y-axis waist positions indicates that the beam is astigmatic. This may also result from deviations from a pure TEM_{00} mode. However, for the purpose of designing the telescope, precise waist parameters are not critical; approximate values are sufficient to guide initial lens placement. Final alignment and optimization are performed experimentally after assembly.

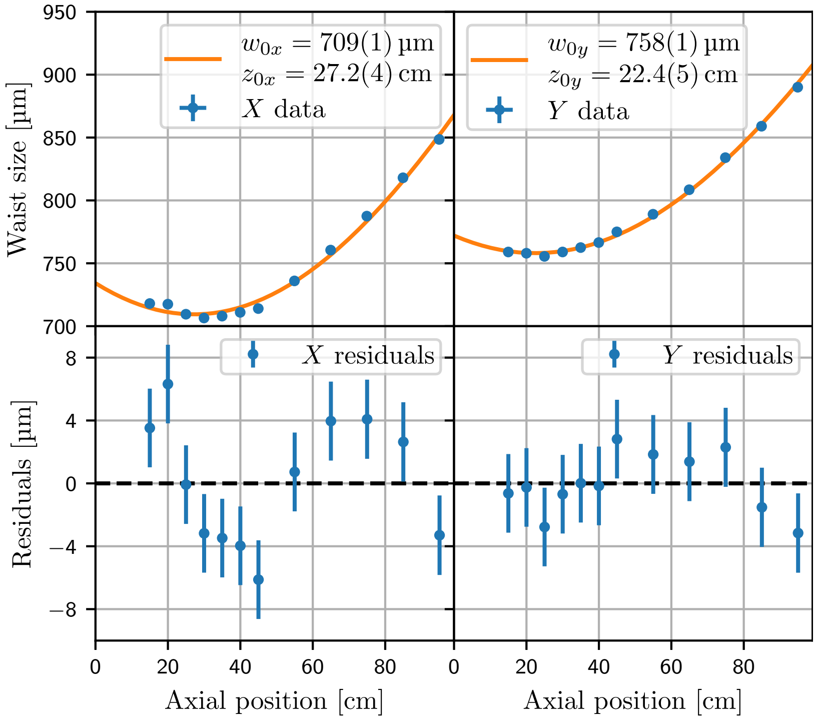

Figure 3.2: Spot size measurements along the propagation axis of the beam emerging from the collimator. The origin is set at a reference hole on the optical table at coordinates (950, 75) in the optical layouts of Figure 3.1, approximately corresponding to the collimator position. Fitted waist parameters indicate that the beam is elliptical and astigmatic. Source code available.

3.2 Power control system

The power control system is placed immediately after the fiber-optic output. This prevents excessive optical power from passing through the downstream lenses when unnecessary, and to avoid variations in spot size on the PBS caused by the movable lens, which may affect its transmittance.

The first component of the system is a crystalline quartz zero-order HWP. A zero-order HWP introduces an optical path length difference of $(m+\frac{1}{2})\lambda$ with $m = 0$ between two orthogonally polarized components of wavelength λ. Compared to multi-order wave plates, zero-order HWPs exhibit lower sensitivity to temperature and wavelength variations. For a linearly polarized input beam, rotation of the HWP controls the output polarization: the angle between input and output polarizations equals twice the angle between the incident polarization and the wave plate axis, as illustrated in Figure 3.3. The HWP is mounted in a motorized rotation stage which can rotate the HWP by steps of $25''$.

Following the HWP, a PBS separates orthogonal polarization components, enabling modulation of the transmitted optical power. The PBS transmits the p-polarized component while reflecting the s-polarized component, with an extinction ratio of 3000 : 1. The reflected beam is directed into a beam dump to prevent back-reflections and unwanted propagation.

According to Malus's law, the transmitted power through the HWP–PBS system is given by

$$P = P_0 \left[\cos^2(\theta_{\text{in}} + 2(\theta_{\text{HWP}} - \theta_{\text{in}})) + \varepsilon\right], \tag{3.1}$$

where θ_{in} and θ_{HWP} denote the polarization angle of the incoming beam and the orientation of the HWP axis, respectively, both referenced to the horizontal. The term ε accounts for the partial polarization of the laser beam and the non-ideal extinction ratio of the PBS. Equation 3.1 could be used to determine the power incident on the sample. However, the HWP motor may occasionally miss steps, causing the actual power to deviate unpredictably. For this reason the optical power is actively monitored using a beam sampler and a monitoring photodiode.

The PBS is made of UV-grade fused silica, whose wavelength-dependent refractive index is described by the Sellmeier equation [34] for the range $0.21\,\mu\text{m} < \lambda < 3.71\,\mu\text{m}$:

$$n^2 - 1 = \frac{0.696\,166\,3\,\lambda^2}{\lambda^2 - (0.068\,404\,3\,\mu\text{m})^2} + \frac{0.407\,942\,6\,\lambda^2}{\lambda^2 - (0.116\,241\,4\,\mu\text{m})^2} + \frac{0.897\,479\,4\,\lambda^2}{\lambda^2 - (9.896\,161\,\mu\text{m})^2}. \tag{3.2}$$

At $\lambda = 1550\,\text{nm}$, the refractive index is approximately $n \approx 1.45$, which increases the optical path length within the PBS cube and is accounted for in the telescope design.

The beam sampler used for optical power monitoring is placed immediately after the PBS. It is designed to minimize wavefront distortion: the downstream surface is wedged to prevent internal fringes, and coated to reduce ghost reflections. The beam sampler relies on Fresnel reflection from an uncoated optical surface, reflecting between 1 % and 10 % of the incident light depending on polarization. Because the polarization state influences the sampler reflectance, the HWP used for polarization control—though not implemented within this thesis—needs to account for this dependence. Owing to space constraints, the incidence angle is set to 28°, where the reflectance is 2.16 % for p-polarized light and 4.53 % for s-polarized light.

The photodiode used for power monitoring has an active area of 5.0 mm in diameter, sufficiently large to capture most of the beam irradiance. Its specified responsivity at 1550 nm is $0.85\,\text{A}\,\text{W}^{-1}$. However, to account for all contributing effects, the relationship between the recorded photodiode voltage and the actual power delivered to the sample is experimentally determined in Section 4.2.

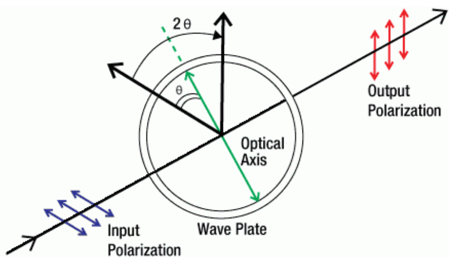

Figure 3.3: Operating principle of a half-wave plate (HWP). Source: [35].

3.3 Telescope

Once the collimated beam is characterized and the optical path length through the PBS determined, the telescope can be designed. The objective is to achieve spot sizes on the sample (located approximately 3 m from the source) ranging from 400 µm to 2000 µm by varying the position of one lens by a few centimeters. At the same time, clipping losses on all optics must remain below the target value of 10^{-6}. All optical components have a clear aperture of 25.4 mm (1″) except for the beam dump, which has an aperture of 11 mm.

A set of plano-convex, thick lenses with focal lengths of 50 mm, 100 mm, 200 mm, and 300 mm was available for constructing the telescope. Their geometry is shown in Figure 3.4, with specifications listed in Table 3.1. The feasible lens combinations and placements are constrained by the limited space on the optical table (Figure 3.1a).

The design process employed the simulation software JamMt [36], which computes Gaussian beam propagation under the paraxial approximation (as described in Section 2.1.2) and outputs lens configurations satisfying the required beam waist evolution. Additional considerations such as clipping and mechanical housing constraints were evaluated manually after the simulations. The input beam to the software was assumed to have a circular cross-section, with parameters taken as the average of the measured values shown in Figure 3.2: $w_0 = 734\,\mu\text{m}$ and $z_0 = 24.8\,\text{cm}$.

The selected lens configuration is reported in Table 3.2. To minimize spherical aberrations, each lens is oriented with its curved surface facing the side with lower beam convergence. Translating Lens 2 by about 2 cm tunes the spot size on the sample across the target range, while keeping clipping losses below 10^{-6} for all elements, as shown in Figures 3.5 and 3.6.

Figure 3.5 shows the expected spot size on the sample and beam dump as a function of the absolute position z_{abs} of Lens 2, measured with respect to the reference hole at the collimator. The micrometer on the translation stage reports a relative position z_{rel}, related to z_{abs} by

$$z_{\text{abs}} = 28.2\,\text{cm} - z_{\text{rel}}. \tag{3.3}$$

The minimum spot size on the sample (369 µm) occurs with Lens 2 placed at $z_{\text{abs}} = 27.2\,\text{cm}$ ($z_{\text{rel}} = 10.0\,\text{mm}$), while the maximum (1880 µm) occurs at $z_{\text{abs}} = 25.2\,\text{cm}$ ($z_{\text{rel}} = 30.0\,\text{mm}$). Discrete points appear in the plot because the software does not support exporting spot size as a function of lens position. An analytical dependence could be derived by writing the ray transfer matrix of the system with Lens 2 position as a parameter.

Figure 3.6 shows the clipping factor on the beam sampler, Lens 3, and the beam dump as Lens 2 is translated. The spot size on all optics is less than that on Lens 3, therefore clipping on all other 1″ optics is not reported. The beam sampler is an exception, as its tilt of 28° reduces its effective aperture relative to the incoming beam.

The clipping factor is computed by integrating the Gaussian irradiance (Equation 2.12) over the aperture of the optical element, Σ, yielding the transmitted power, P_{tr}, and the corresponding clipping ratio,

$$\eta = 1 - \frac{P_{\text{tr}}}{P_{\text{tot}}} = 1 - \frac{\int_\Sigma I(x,y,z)\,\mathrm{d}x\mathrm{d}y}{\int_{\mathbb{R}^2} I(x,y,z)\,\mathrm{d}x\mathrm{d}y}. \tag{3.4}$$

For a circular aperture of radius R oriented perpendicular to the propagation direction, and assuming perfect alignment of the aperture with the optical axis, this expression reduces to

$$\eta = \exp\left(-\frac{2R^2}{w^2(z)}\right). \tag{3.5}$$

For the tilted beam sampler, the clipping factor can be approximated by using the same expression, but with an effective aperture radius $R' = R\cos\theta$, where $\theta = 28°$ is the tilt angle of the surface. This adjustment accounts for the geometric reduction in the projected area of the aperture as seen by the incoming beam.

Table 3.1: Specifications of the available plano-convex lenses. Quantities are defined in Figure 3.4. Simulation software JamMt supports specifying center thickness, focal length, and radii of curvature.

Manufacturer	Model	Focal length (mm)	Radius of curvature (mm)	Center thickness (mm)	Edge thickness (mm)	Back focal length (mm)
Thorlabs	LA4148	50.2	23.0	5.8	2.1	46.2
Thorlabs	LA4380	100.3	46.0	3.8	2.1	97.7
Thorlabs	LA4102	200.7	92.0	2.9	2.0	198.7
Thorlabs	LA4579	301.1	138.0	2.6	2.0	299.3

Table 3.2: Selected lens configuration. Positions are given relative to the reference hole at the collimator.

Lens ID	Focal length (mm)	Position (cm)
Lens 1	50	15
Lens 2	200	25.2–27.2
Lens 3	300	50

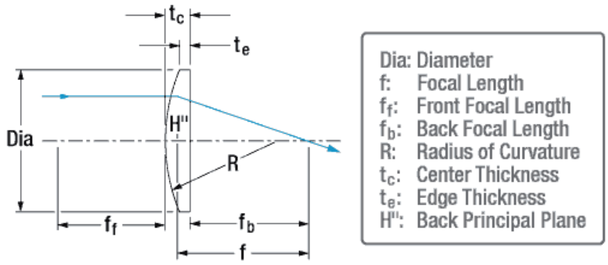

Figure 3.4: Geometrical diagram of the available plano-convex lenses. Source: [35].

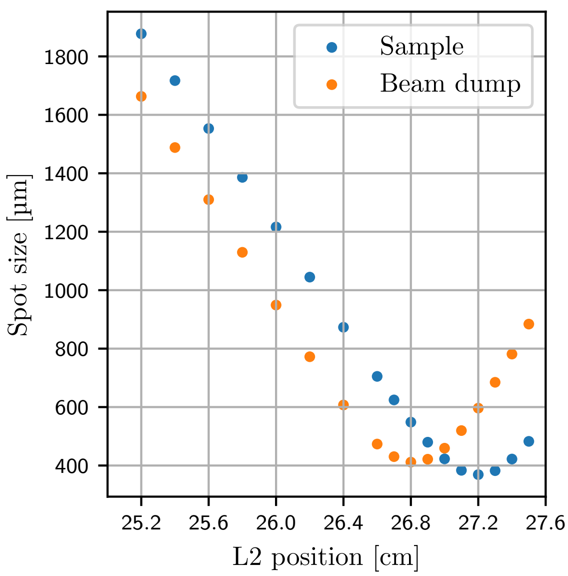

Figure 3.5: Simulated spot size on the sample and terminating dump as a function of Lens 2 position. The sample is assumed at 2.985 m from the reference hole, while the beam dump at 3.26 m. The minimum spot size at the sample is 369 µm with Lens 2 at $z_{\text{abs}} = 27.2$ cm, while the maximum is 1880 µm at $z_{\text{abs}} = 25.2$ cm. Source code available.

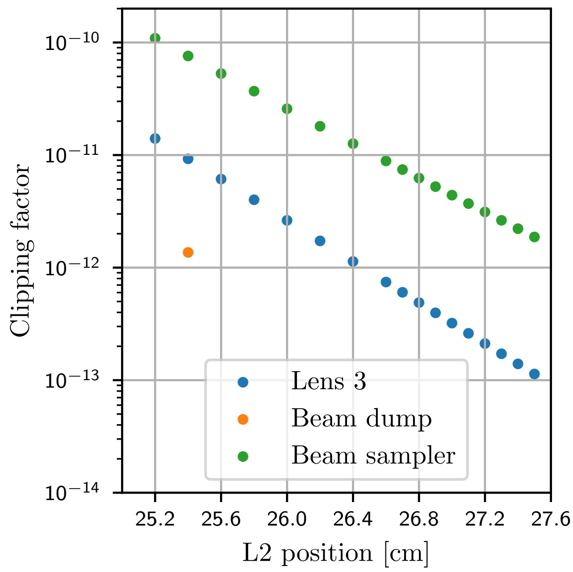

Figure 3.6: Simulated clipping factors for the beam sampler, Lens 3, and the terminating dump as a function of Lens 2 position. Clipping for all other elements is smaller than that on Lens 3. The beam dump has a diameter of 11 mm, while other optics have a diameter of 25.4 mm (1″). Expected clipping on the beam dump falls below 10^{-14} for z_{abs} between 25.5 cm and 27.2 cm. Source code available.

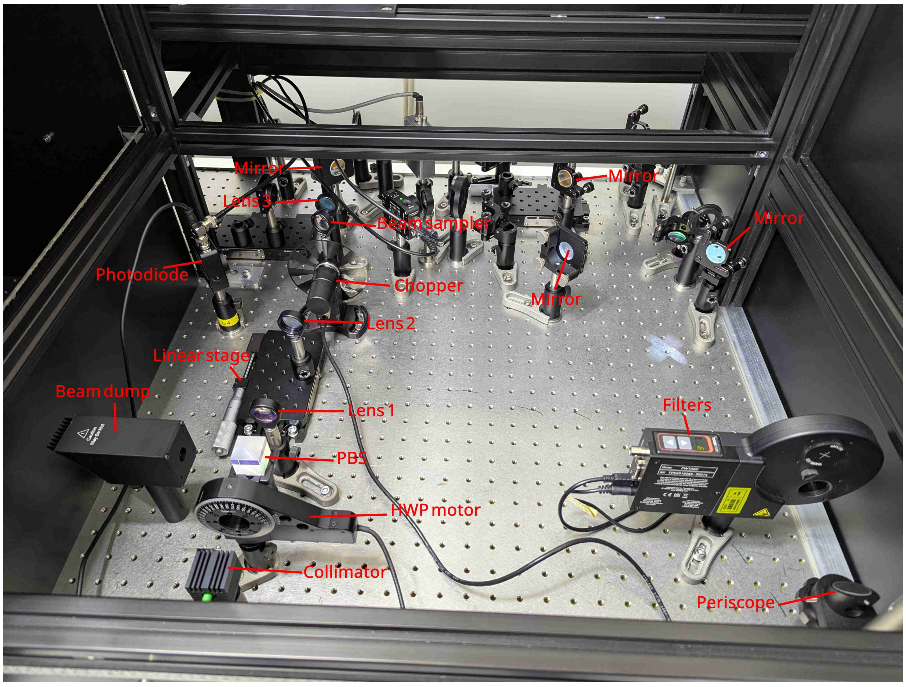

Figure 3.7: Final laser line constructed as part of this thesis. All components relevant to the 1550 nm line are labeled.

3.4 Measurement system

The laser beam is directed toward the scatterometer through a sequence of dielectric mirrors (cM1, cM2, cM3, and cFM4 in Figure 3.1b), and a periscope. The periscope consists of two vertically aligned mirrors that raise the beam by about 20 cm, matching the height required by the scatterometer. Figure 3.7 shows the completed bottom floor of the facility that has been built as part of this thesis.

Because it is shared by all laser lines, the periscope uses metallic mirrors, which provide a broader spectral range than dielectric mirrors, although with slightly lower reflectance. Both metallic and dielectric mirrors are specified to have reflectance exceeding 99 %, thus six mirrors in the beam path result in a total relative power loss of at most 5.9 %.

All mirrors are mounted in kinematic mounts equipped with fine adjustment screws, enabling precise beam steering and alignment. These adjustments are used to minimize clipping and ensure that the beam is centered on the desired surface element of the sample. The sample itself is mounted on a holder that provides both vertical and horizontal positioning. At present, the scatterometer measures scattered power only in the horizontal plane containing the incident beam. For accurate measurement, the illuminated surface element must be centered on the photodetector rotation axis.

To enable measurements at small scattering angles, light is not collected directly by the photodetector. Instead, a prism mirror located 25.4 cm from the rotation axis reflects the scattered light upward to the photodetector, which is mounted above the prism mirror and rotates with it, as illustrated in Figure 3.8. Because the prism is only 3 mm wide, the setup permits measurements at angles as small as 0.7°. Placing the detector directly in the scattering plane would otherwise block these measurements due to the housing size.

The photodetector has an extremely high sensitivity and a low damage threshold (10 mW), which limits the maximum input power. To prevent saturation or damage, neutral density filters can be placed before the detector; their optical densities are experimentally measured in Section 4.4. An iris diaphragm is also present to reduce the field-of-view of the detector and reduce measured stray light.

To enhance sensitivity, lock-in detection is employed. The incident beam is modulated at 23 Hz using a mechanical chopper, producing a square-wave signal. The lock-in amplifier receives both the photodetector output and the reference waveform, rejecting noise components not synchronized with the modulation frequency. It is configured with a time constant of 300 ms (corresponding to a cutoff frequency of 0.5 Hz) and a roll-off of 12 dB oct^{-1}. Although a narrow band-pass filter centered at

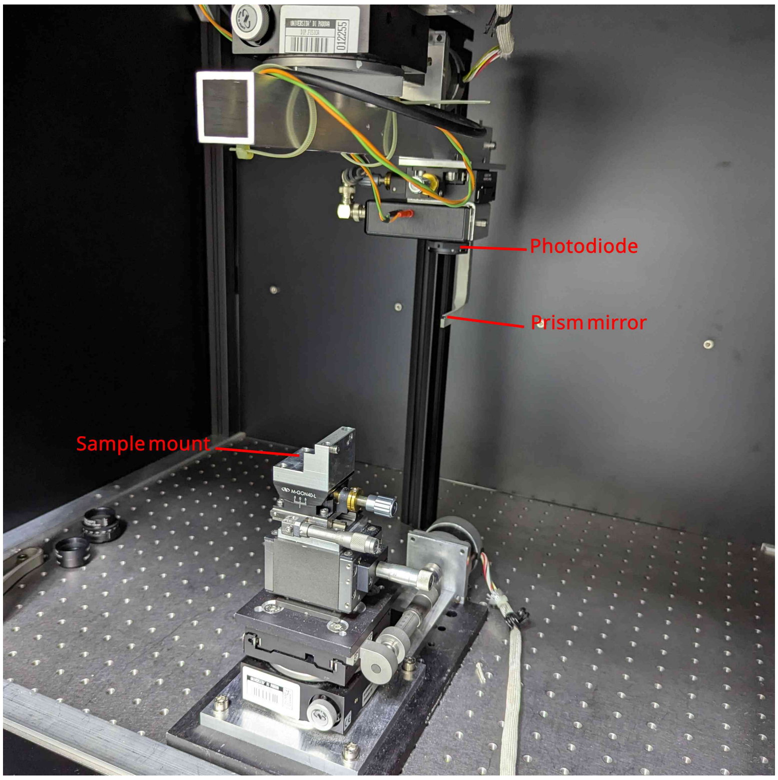

Figure 3.8: Scatterometer setup. The image shows the sample holder and the rotating arm with the prism mirror and photodetector used for measuring scattered light.

1550 nm could further reduce background noise, it was not available during the present work.

The scatterometer is operated using custom software that controls motorized positioning, regulates incident power, and manages data acquisition. During a measurement, the software moves the photodetector arm across the scattering plane to sample the angular distribution of scattered light. The software also rotates the HWP to regulate the incident power, preventing saturation of either the photodetector or the lock-in amplifier, whose maximum input voltage is 1 V. Conversion of the recorded voltages into BSDF values requires calibration, as detailed in Section 4.2.

Chapter 4

Laser Line Characterization

Following its construction and alignment, the laser line is experimentally characterized, and the results are compared with the design expectations.

This chapter presents the characterization of the beam in the scatterometer area as Lens 2 position is varied, and the effective power delivered to the sample as a function of the HWP angle. The power-monitor photodiode is calibrated to determine the conversion factor between the recorded voltage and the actual optical power at the sample. Additionally, the contributions of electronic noise and stray-light background to the measurement system are quantified. Finally, the characterization is completed by measuring the BRDF of a reference sample with a known scattering profile.

4.1 Output beam characterization

The beam in the scatterometer area was characterized using the beam profiler. Beam spot sizes along the X and Y axes were measured at multiple axial positions for different positions of Lens 2. The measurements are fitted using Gaussian beam propagation theory, yielding estimates of the beam waist sizes and positions, as well as the spot sizes at the sample and beam dump. In addition, the Y-centroid of the beam was recorded to monitor beam alignment. The measured spot sizes are summarized in Table 4.1 and illustrated in Figure 4.1. The origin of the z-axis is set at coordinates (700, 75) in the optical layouts of Figure 3.1, corresponding approximately to the location of an iris diaphragm.

The sample is located at approximately 30 cm from the reference, and the beam dump at 57.5 cm. As expected from the optical design, the spot sizes at the sample range from approximately 390 µm to 1970 µm. The beam is elliptical and astigmatic, consistent with the input beam characteristics after the collimator, as discussed in Section 3.1. At the beam dump, the spot sizes reach up to 1900 µm, which corresponds to roughly one-third of the dump aperture radius of 5500 µm.

The measured Y-centroids are shown in Figure 4.2. These measured values were relative to an arbitrary zero set by the beam profiler's support height. For clarity, the plotted values are shifted such that the Y-centroid of the beam of largest spot size at the dump (Lens 2 at 30 mm) is zero. On the beam dump, the centroid varies by approximately 800 µm across the full range of Lens 2 positions. To minimize clipping across this range, the beam dump is aligned with the beam of largest spot size. The resulting clipping factors are estimated by numerical integration of Equation 3.4 to account for this offset. Despite the offset, all clipping factors remain below 10^{-12}. This analysis considers only vertical tilt, since the vertical reference is reproducible when the beam profiler is moved along the z-axis due to its fixed support height. Horizontal tilt was not measured, as it requires a different procedure to ensure reproducible horizontal referencing when repositioning the profiler.

Table 4.1: Fitted beam waist parameters along the X and Y axes for different Lens 2 positions, with corresponding spot sizes at the sample and beam dump. Axial positions are given relative to a reference hole in the optical table, corresponding to the iris diaphragm at coordinates (700, 75) in the optical layouts of Figure 3.1.

	Waist parameters				Sample		Beam dump	
L2 pos. (mm)	w_{0x} (µm)	z_{0x} (cm)	w_{0y} (µm)	z_{0y} (cm)	X size (µm)	Y size (µm)	X size (µm)	Y size (µm)
10.0	377(2)	34.2(2)	371.2(2)	41.3(2)	381(2)	401(2)	485(2)	429(1)
12.5	401(2)	54.9(2)	418.7(2)	63.5(2)	505(2)	576(2)	402(2)	425(2)
15.0	445(2)	79.0(2)	476.8(3)	90.1(2)	703(2)	784(1)	505(2)	584(2)
20.0	542(4)	138.1(5)	616.7(4)	159.9(6)	1123(1)	1208(1)	912(2)	1025(2)
25.0	674(5)	221(1)	735.5(6)	243(1)	1551(1)	1608(1)	1372(2)	1446(2)
30.0	824(8)	327(2)	985(11)	374(3)	1958(1)	1984(1)	1810(2)	1866(2)

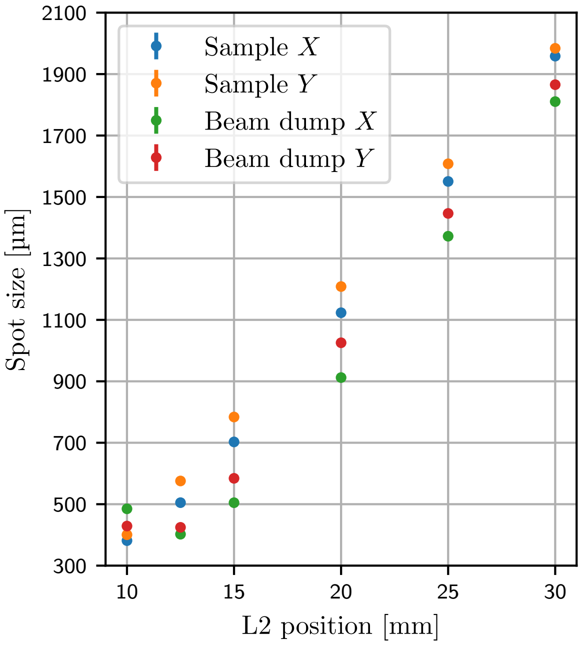

Figure 4.1: Spot sizes at the sample and beam dump for different Lens 2 positions. The sample is located at 30 cm from the reference, and the beam dump at 57.5 cm. Source code available.

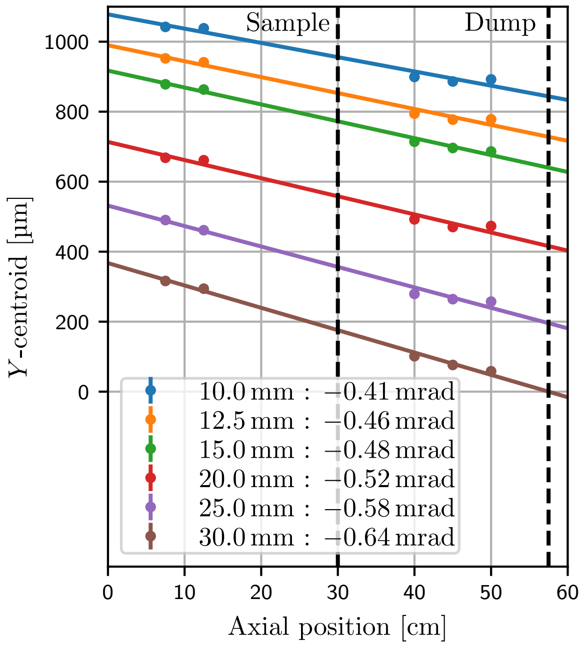

Figure 4.2: Y-centroids as a function of Lens 2 position. The centroid is defined to be zero at the beam dump when Lens 2 is at 30 mm. For each Lens 2 position the tilt is reported. Source code available.

4.2 Power characterization

Accurate characterization of the optical power delivered to the sample requires calibration of the photodetector used for power monitoring. This calibration establishes the mapping between the detector's voltage output and the actual optical power incident on the sample.

Optical powers are measured using a power sensor, which the manufacturer specifies to have an uncertainty of ±5 %. This uncertainty is significantly larger than the observed statistical fluctuations in repeated measurements and is therefore treated as a correlated systematic error. Consequently, fits are performed without assigning individual point-by-point uncertainties, and the posterior uncertainty is estimated from the fitted data. The specified systematic uncertainty must be considered when reporting absolute power values, although it does not affect relative comparisons within the same measurement session.

Before performing the detector calibration, consistency checks were performed by verifying the expected dependence of the transmitted power on the HWP angle and by quantifying optical losses in the beam path. Figure 4.3 shows the optical power measured at the sample as a function of the HWP angle reported by the motor. The data are in excellent agreement with the theoretical dependence predicted by Malus's law (Equation 3.1). The HWP motor resolution is $25''$ thus the uncertainty in the angle is neglected. However, across different measurement sessions the motor may occasionally miss steps, which prevents accurate reproducibility of the absolute angular position. For this reason, continuous power monitoring with the photodetector is required.

For selected HWP angles, the optical power was measured at three different positions in the beam path corresponding to the power incident on the beam sampler (P_{BS}), on the photodetector (P_{PD}), and on the sample (P_{s}). The fractional loss in the optical path is then computed as

$$\eta_{\mathrm{loss}} = 1 - \frac{P_{\mathrm{s}} + P_{\mathrm{PD}}}{P_{\mathrm{BS}}}. \tag{4.1}$$

Figure 4.4 shows that the total optical losses amount to approximately 5.4 % of the circulating power, which is slightly below the upper bound of 5.9 % estimated in Section 3.4 based on the reflectance of the mirrors in the beam path.

The calibration curve relating the photodetector voltage to the optical power incident on the sample is shown in Figure 4.5. A linear fit to the data yields a conversion factor of 46.84(7) mW V^{-1}, whose uncertainty does not include the 5 % systematic uncertainty of the power sensor. The coefficient of determination R^2 exceeds 0.9999, confirming the linearity of the detector response across the calibration range.

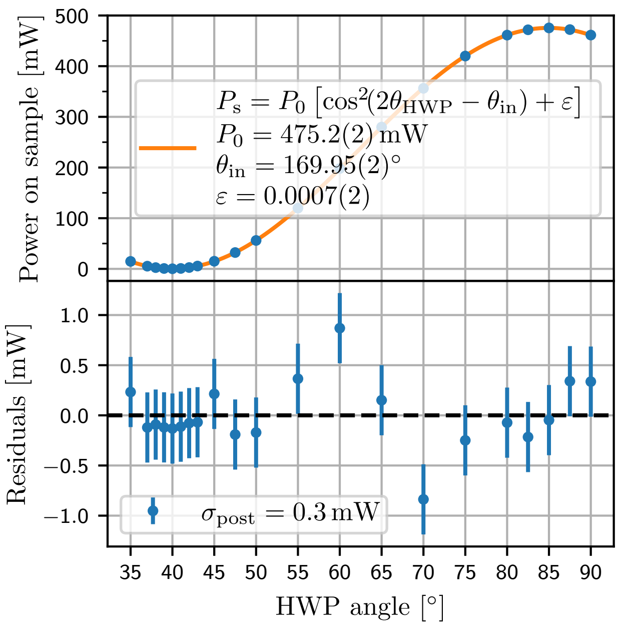

Figure 4.3: Optical power measured at the sample as a function of HWP rotation angle reported by the motor. The fitted curve follows the dependence predicted by Malus's law (Equation 3.1). The uncertainty of P_0 does not include the 5 % systematic uncertainty of the power sensor. Source code available.

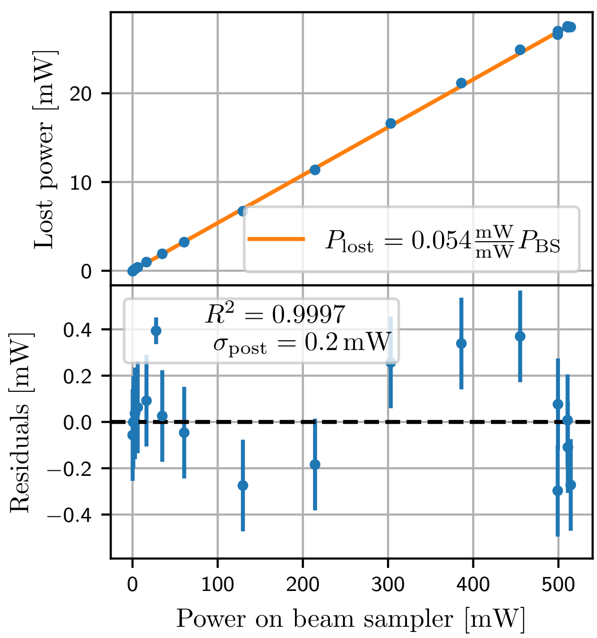

Figure 4.4: Fractional optical power losses in the beam path between the beam sampler and the sample. The measured loss fraction is below the upper bound of 5.9 % estimated in Section 3.4 based on the reflectance of the mirrors in the beam path. Source code available.

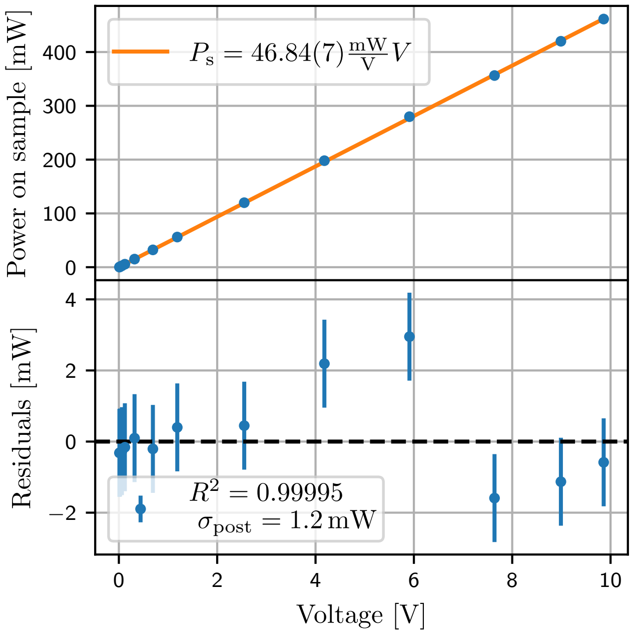

Figure 4.5: Calibration curve relating the photodetector voltage to the optical power incident on the sample. The linear fit provides the calibration factor. Source code available.

4.3 Background noise

Background noise was characterized by operating the scatterometer as in a regular BSDF measurement, but with no sample in place. Measurements were acquired over the full scattering angle range of 0° to 180°, where $\theta_s = 0°$ corresponds to the prism mirror blocking the beam before it reaches the sample, and $\theta_s = 180°$ corresponds to the prism facing both the sample and the incident beam in the same direction.

At each detector position, the acquisition software recorded the voltage of the power-monitor photodiode along with five repeated measurements of the lock-in amplifier output voltage. The input power was automatically adjusted to avoid saturation of either the photodiode (10 mW threshold) or the lock-in amplifier (1 V maximum input). The monitor voltage is converted into optical power using the calibration relation determined in Section 4.2.

In contrast, the scatterometer detector was not fully calibrated due to time constraints. Its output was instead converted to optical power using the nominal transimpedance gain of $2 \times 10^{10}\,\mathrm{V\,A^{-1}}$ and the specified responsivity of $1.04\,\mathrm{A\,W^{-1}}$ at 1550 nm. An additional correction factor arises from the lock-in amplifier when using an external square-wave reference. This was estimated as $0.441\,\mathrm{V\,V^{-1}}$ for the other laser lines in the facility, and is assumed equal for the 1550 nm line. Therefore, the reported background noise values should be regarded as approximate, order-of-magnitude estimates. The 97 % reflectance of the collection prism mirror was also included in the effective detected power.

The active area of the photodetector is 1 mm in diameter and positioned at a distance of 25.4 cm from the beam, corresponding to a solid angle of 1.2×10^{-5} sr.

The acquisition software recorded both the high and low voltages of the power-monitor photodiode as the beam was modulated by the chopper. Occasional artifacts appeared in these readings due to the relatively long chopping times. To mitigate this, the chopper blade will be replaced with one containing fewer slots, thereby increasing the modulation period. For the present analysis, these artifacts—manifesting as spurious decreases in the high voltage and increases in the low voltage—were suppressed by retaining only the maximum high voltage and minimum low voltage from each measurement set.

The background noise level can be further reduced by optimizing the beam dump height as described in Section 4.1, and by adjusting the aperture of the iris placed between the periscope and the sample. With these optimizations, the noise floor is sufficiently low for the experimental requirements.

Figure 4.6 shows the equivalent cBSDF of the electronic noise, the measured background noise for three Lens 2 positions, and a theoretical expectation curve.

Electronic noise was measured by blocking the beam before it entered the periscope, thereby preventing stray light from originating in the sample area. The equivalent cBSDF of this noise depends on the input power, as given by Equation 2.23. Because the input power was essentially identical at a given detection angle for all three background curves, only one electronic noise curve is plotted. The electronic noise cBSDF remains below $10^{-8}\,\mathrm{sr}^{-1}$, indicating a very low contribution to the overall measurements.

The theoretical noise model of Equation 2.24, originally developed for the other laser lines in the facility [30, 31], is also included. The model was adapted to the new wavelength and assumes a fixed beam under the geometrical optics approximation. In practice, however, the plot shows that the noise BSDF depends on the position of Lens 2. As discussed in Section 4.1, translating Lens 2 modifies the beam spot size at a given axial position, and introduces vertical and horizontal shifts and tilts. These effects are not captured by the simple model, and a more advanced treatment would be required to fully explain the observed dependence.

The theoretical curve indicates that background noise could be reduced by an order of magnitude, perhaps by minimizing stray light further. Nevertheless, the measured background noise cBSDF remains below $10^{-6}\,\mathrm{sr}^{-1}$ at most scattering angles, which is sufficiently low to enable accurate measurement of the scattering properties of most materials.

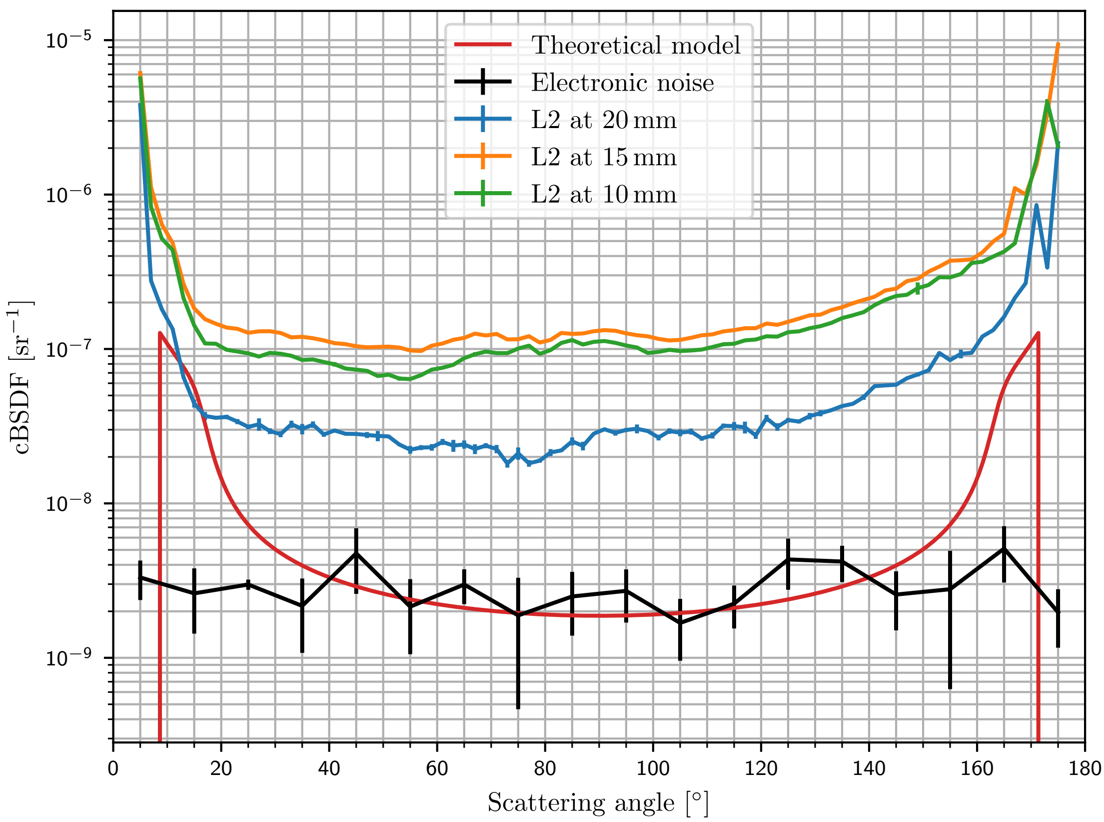

Figure 4.6: Measured background noise and electronic noise, compared with the theoretical model curve. The scattering angle $\theta_\mathrm{s} = 0°$ corresponds to the prism mirror blocking the beam before it reaches the sample, while $\theta_\mathrm{s} = 180°$ is the opposite orientation. The three background curves correspond to different Lens 2 positions. Only one electronic noise curve is shown, since the input power for the three background curves is practically identical at a given scattering angle. The theoretical curve is based on a Rayleigh scattering model developed for the other laser lines in the facility [30, 31]. Source code available.

4.4 Reference sample analysis

To validate the measurement setup, a Spectralon reference sample was characterized. Spectralon is a nearly ideal Lambertian reflector with an albedo of 0.99. A Lambertian surface is a diffuse reflector whose radiance is isotropic, meaning that incident light is scattered equally in all directions.

The BRDF of a Lambertian reflector is constant and can be directly related to the surface albedo ρ. The reflected fraction of incident light can be expressed as the integral of the BRDF over the reflection hemisphere Ω:

$$\rho = \int_\Omega \mathrm{BRDF} \cos\theta_\mathrm{s} \mathrm{d}\Omega = \mathrm{BRDF} \int_\Omega \cos\theta_\mathrm{s} \mathrm{d}\Omega = \mathrm{BRDF} \cdot \pi \text{ sr}, \tag{4.2}$$

where $\cos\theta_\mathrm{s}$ accounts for the projected area of the surface element when computing irradiance contributions from different scattering angles. From this, the expected BRDF of the reference sample is

$$\frac{0.99}{\pi \text{ sr}} = 0.315\,\mathrm{sr}^{-1}.$$

The BRDF of the Spectralon surface was measured using the scatterometer over the angular ranges $-90°$ to $-1°$ and $1°$ to $90°$. Lens 2 was at 10 mm, corresponding to a spot size of about 400 µm on the sample. The measured data are presented in Figure 4.7.

Artifacts observed in the background measurements were again present in these measurements. However, in this case the incident power varied significantly with scattering angle. To mitigate these artifacts, the recorded signal from the power-monitor photodiode was taken as the sum of the high- and low-voltage readings. Notably, the decrease in high-voltage signal closely matched the increase in the low-voltage signal. Since the low-voltage readings are on the order of millivolts, the resulting systematic error is small compared to the uncertainties introduced by the uncalibrated photodetector and the approximate lock-in amplifier conversion factor.

Because the scattered signal from the Spectralon sample was stronger than in the background measurements, neutral density filters NENIR10A-C and NENIR20A-C were used in front of the photodetector to prevent saturation. Their measured optical densities, along with those of additional filters available for more reflective samples, are listed in Table 4.2.

At scattering angles near $\pm 90°$, the computed BRDF diverges because the measured scattered power does not approach zero due to background noise. Additionally, at angles below $-75°$, the sample holder introduces a shadow that reduces the measured scattered power, resulting in artificially low BRDF values. Therefore, these angular ranges were excluded from the analysis. Over the remaining angular range of $-75°$ to $85°$, the mean BRDF is computed as

$$\mathrm{BRDF} = 0.27(1)\,\mathrm{sr}^{-1}.$$

This measured value is in reasonable agreement with the expected $0.315\,\mathrm{sr}^{-1}$, corresponding to a deviation of approximately 14 %. Given the missing photodetector calibration and the approximate lock-in conversion factor, this level of agreement is considered satisfactory for validating the measurement setup and confirming the reliability of the scatterometer for subsequent sample measurements.

Table 4.2: Measured optical densities of the filters available to measure intense scattered light measurements. The nominal damage threshold at 1550 nm is also reported where available.

Manufacturer	Model	Optical Density at 1550 nm	Damage Threshold at 1550 nm ($\mathrm{W\,cm^{-1}}$)
Thorlabs	NENIR10A-C	0.906	72.8
Thorlabs	NENIR20A-C	1.893	–
Thorlabs	NENIR40A-C	3.822	58.3
Thorlabs	NENIR60A	5.713	15

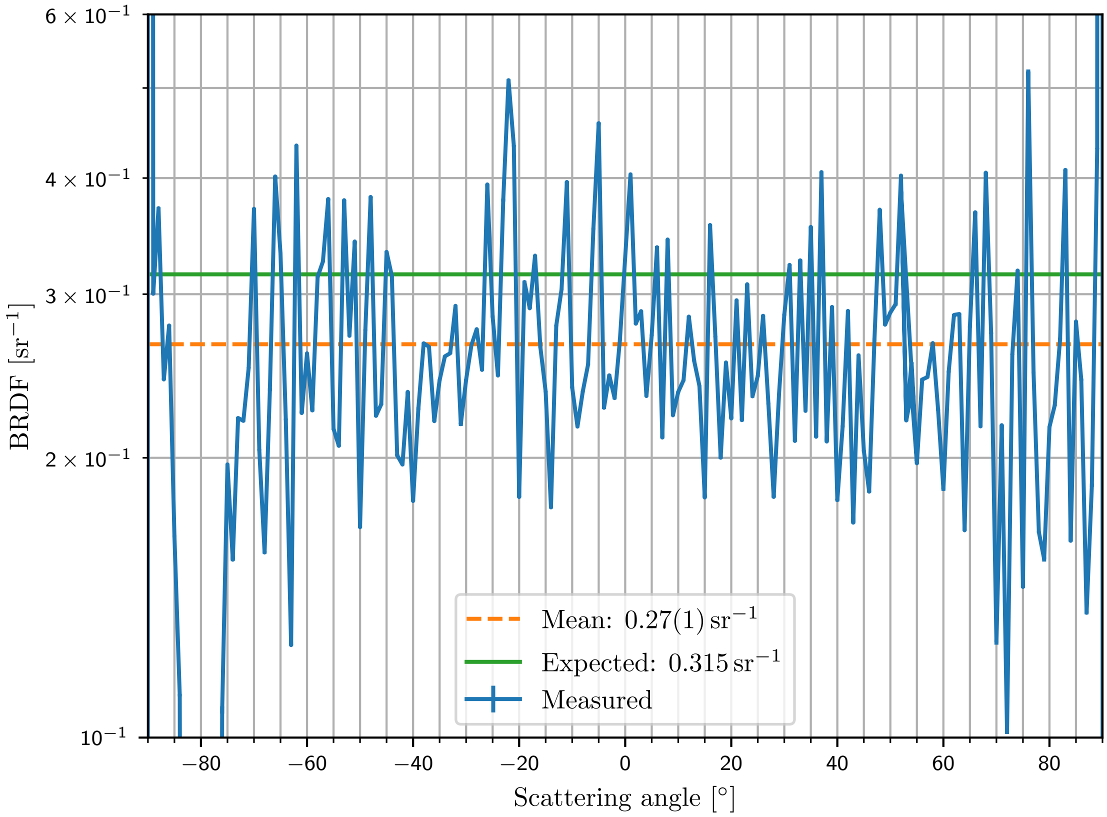

Figure 4.7: Measured BRDF of the Spectralon reference sample. The measured BRDF is in reasonable agreement with the expected value, taking into account the uncalibrated photodetector and the approximate lock-in amplifier conversion factor. Source code available.

Chapter 5

Conclusions

This work establishes a fully operational laser line at 1550 nm for the experimental characterization of optical materials and coatings relevant to the low-frequency detector of the upcoming Einstein Telescope. The system integrates seamlessly into the existing infrastructure, which hosts other laser lines used for testing materials in current gravitational-wave detectors.

The facility characterizes scattering properties using a scatterometer, which measures the bidirectional scattering distribution function (BSDF), and an integrating sphere, which measures total integrated scatter (TIS). This thesis focuses on the development and implementation of the new laser line for scatterometer measurements.

The laser line enables precise beam steering toward the sample, with accurate control of both power and spot size. Beam characterization and telescope design confirm that spot sizes on the sample range from approximately 400 µm to 2000 µm, in agreement with expectations. The telescope, built from plano-convex lenses, allows fine adjustment of the spot size while maintaining negligible clipping on optical elements.

Power regulation and monitoring are achieved using a half-wave plate and a polarizing beam splitter, enabling continuous control from near zero up to approximately 500 mW. Calibration of the monitoring photodiode provides a reliable conversion between measured voltage and the power delivered to the sample. Total optical losses along the beam path remain below 5.5 %, consistent with design expectations.

Noise characterization confirm that background contributions from electronic noise and stray light are sufficiently low for accurate BSDF measurements. Beam modulation and lock-in demodulation, combined with careful alignment and the use of absorptive panels and beam dumps, effectively suppresses both electronic and optical noise.

Validation using a Spectralon reference sample demonstrates that the scatterometer produces BRDF measurements in good agreement with theoretical expectations. The measured mean BRDF of $0.27(1)\,\mathrm{sr}^{-1}$ closely approaches the expected value of $0.315\,\mathrm{sr}^{-1}$, given the approximate calibration of the photodetector and lock-in amplifier. Completion of the calibration will further enhance measurement accuracy. These results confirm that the system is capable of producing accurate BSDF measurements for characterizing candidate materials and coatings for the Einstein Telescope.

Future work will focus on integrating the laser line with the existing TIS measurement system. This will require routing the beam to the TIS setup, along with minor adjustments and verification tests. Once completed, the facility will provide both BSDF and TIS measurements at 1550 nm, enabling comprehensive characterization of scattering properties for next-generation gravitational-wave detectors.

Bibliography

[1] D. Castelvecchi. "Gravitational waves: How LIGO forged the path to victory". In: *Nature* 530.7590 (Feb. 2016), pp. 261–262. DOI: 10.1038/530261a.

[2] B. P. Abbott et al. "Observation of gravitational waves from a binary black hole merger". In: *Physical Review Letter* 116.6 (Feb. 2016), p. 061102. DOI: 10.1103/PhysRevLett.116.061102.

[3] A. Abac et al. *The science of the Einstein Telescope*. Mar. 2025. arXiv: 2503.12263 [gr-qc].

[4] F. Sorrentino. "The Advanced Virgo interferometer". In: *2016 IEEE Metrology for Aerospace*. Sept. 2016, pp. 251–254. DOI: 10.1109/MetroAeroSpace.2016.7573221.

[5] J. Harms. "Terrestrial gravity fluctuations". In: *Living Reviews in Relativity* 22.6 (Oct. 2019). DOI: 10.1007/s41114-019-0022-2.

[6] D. Fiorucci et al. "Impact of infrasound atmospheric noise on gravity detectors used for astrophysical and geophysical applications". In: *Physical Review D* 97 (6 Mar. 2018), p. 062003. DOI: 10.1103/PhysRevD.97.062003.

[7] J. Harms and K. Venkateswara. "Newtonian-noise cancellation in large-scale interferometric GW detectors using seismic tiltmeters". In: *Classical and Quantum Gravity* 33.23 (Oct. 2016), p. 234001. DOI: 10.1088/0264-9381/33/23/234001.

[8] G. Hammond and S. Rowan. "Thermal noise, suspensions and new materials". In: *2014 IEEE Metrology for Aerospace*. May 2014, pp. 515–520. DOI: 10.1109/MetroAeroSpace.2014.6865979.

[9] L. Barsotti, J. Harms, and R. Schnabel. "Squeezed vacuum states of light for gravitational wave detectors". In: *Reports on Progress in Physics* 82.1 (Dec. 2018), p. 016905. DOI: 10.1088/1361-6633/aab906.

[10] J. Y. Vinet, V. Brisson, and S. Braccini. "Scattered light noise in gravitational wave interferometric detectors: Coherent effects". In: *Physical Review D* 54.2 (July 1996), pp. 1276–1286. DOI: 10.1103/PhysRevD.54.1276.

[11] J. Y. Vinet et al. "Scattered light noise in gravitational wave interferometric detectors: A statistical approach". In: *Physical Review D* 56.10 (Nov. 1997), pp. 6085–6095. DOI: 10.1103/PhysRevD.56.6085.

[12] ET Steering Committee Editorial Team. *Einstein Telescope: Design report update 2020*. Technical Report ET-0007B-20. Nov. 2020. URL: https://gwic.science/3Gsubcomm/docs/ET-0007B-20_ETDesignReportUpdate2020.pdf (visited on Sept. 1, 2025).

[13] S. Hild et al. "A xylophone configuration for a third-generation gravitational wave detector". In: *Classical and Quantum Gravity* 27.1 (Dec. 2009), p. 015003. DOI: 10.1088/0264-9381/27/1/015003.

[14] S. Rowlinson and others. "Feasibility study of beam-expanding telescopes in the interferometer arms for the Einstein Telescope". In: *Physical Review D* 103.2 (Jan. 2021), p. 023004. DOI: 10.1103/PhysRevD.103.023004.

[15] L. Pinard et al. "Mirrors used in the LIGO interferometers for first detection of gravitational waves". In: *Applied Optics* 56.4 (Feb. 2017), pp. C11–C15. DOI: 10.1364/AO.56.000C11.

[16] D. F. McGuigan et al. “Measurements of the mechanical Q of single-crystal silicon at low temperatures”. In: *Journal of Low Temperature Physics* 30.5 (Mar. 1978), pp. 621–629. DOI: 10.1007/BF00116202.

[17] J. Degallaix et al. “Bulk optical absorption of high resistivity silicon at 1550 nm”. In: *Optics Letters* 38.12 (June 2013), pp. 2047–2049. DOI: 10.1364/OL.38.002047.

[18] C. Krüger et al. “Birefringence measurements on crystalline silicon”. In: *Classical and Quantum Gravity* 33.1 (Dec. 2015), p. 015012. DOI: 10.1088/0264-9381/33/1/015012.

[19] A. D. Bristow, N. Rotenberg, and H. M. van Driel. “Two-photon absorption and Kerr coefficients of silicon for 850-2200nm”. In: *Applied Physics Letters* 90.19 (May 2007), p. 191104. DOI: 10.1063/1.2737359.

[20] K. G. Lyon et al. “Linear thermal expansion measurements on silicon from 6 to 340 K”. In: *Journal of Applied Physics* 48.3 (Mar. 1977), pp. 865–868. DOI: 10.1063/1.323747.

[21] J. Komma et al. “Thermo-optic coefficient of silicon at 1550 nm and cryogenic temperatures”. In: *Applied Physics Letters* 101.4 (July 2012), p. 041905. DOI: 10.1063/1.4738989.

[22] M. Mehmet and H. Vahlbruch. “High-efficiency squeezed light generation for gravitational wave detectors”. In: *Classical and Quantum Gravity* 36.1 (Dec. 2018), p. 015014. DOI: 10.1088/1361-6382/aaf448.

[23] A. E. Siegman. *Lasers*. University Science Books, 1986. ISBN: 9780935702118.

[24] F. L. Pedrotti, L. M. Pedrotti, and L. S. Pedrotti. *Introduction to Optics*. Third. Cambridge University Press, 2017. ISBN: 9781108428262.

[25] S. Schröder et al. “Modeling of light scattering in different regimes of surface roughness”. In: *Optics Express* 19.10 (May 2011), pp. 9820–9835. DOI: 10.1364/OE.19.009820.

[26] D. Gigilashvili et al. “The role of subsurface scattering in glossiness perception”. In: *ACM Transactions on Applied Perception* 18.3 (May 2021), pp. 1–26. DOI: 10.1145/3458438.

[27] Q. J. Chen. *BSDF (Bidirectional Scattering Distribution Function)*. 2020. URL: https://giaosame.github.io/BSDF/ (visited on Sept. 1, 2025).

[28] C. F. Bohren and D. R. Huffman. *Absorption and scattering of light by small particles*. Wiley, 1983. ISBN: 0471293407.

[29] G. S. Smith. “Human color vision and the unsaturated blue color of the daytime sky”. In: *American Journal of Physics* 73.7 (July 2005), pp. 590–597. DOI: 10.1119/1.1858479.

[30] F. Flocco. “Experimental investigation of stray light from dust contamination in gravitational wave detectors”. Master’s thesis. Università degli Studi di Padova, July 2024. URL: https://hdl.handle.net/20.500.12608/68241.

[31] I. Takimoto Schmiegelow. “Characterizing light scattering sources in gravitational-wave interferometers”. Master’s thesis. Università degli Studi di Padova, Sept. 2023. URL: https://hdl.handle.net/20.500.12608/51841.

[32] Zurich Instruments. *Principles of lock-in detection*. URL: https://www.zhinst.com/ch/en/resources/principles-of-lock-in-detection (visited on Sept. 1, 2025).

[33] R. Schilling. *OptoCad*. Version 0.94a. A Fortran 95 module for tracing Gaussian TEM00 beams through an optical setup.

[34] I. H. Malitson. “Interspecimen comparison of the refractive index of fused silica”. In: *Journal of the Optical Society of America* 55.10 (Oct. 1965), pp. 1205–1209. DOI: 10.1364/JOSA.55.001205.

[35] Throlabs Inc. *Photonics products and solutions*. URL: https://thorlabs.com (visited on Sept. 1, 2025).

[36] A. Thüring and N. Lastzka. *JamMt*. Version 0.24. Just another mode matching tool.